VASCULAR DISEASE

Bioengineered vascular grafts with a pathogenic *TGFBR1* variant model aneurysm formation in vivo and reveal underlying collagen defects

Ying Yang[1], Hao Feng[1,2], Ying Tang[1,2], Zhenguo Wang[3], Ping Qiu[1], Xihua Huang[1], Lin Chang[3], Jifeng Zhang[3], Yuqing Eugene Chen[1,3]*, Dogukan Mizrak[1]*, Bo Yang[1]*

Thoracic aortic aneurysm (TAA) is a life-threatening vascular disease frequently associated with underlying genetic causes. An inadequate understanding of human TAA pathogenesis highlights the need for better disease models. Here, we established a functional human TAA model in an animal host by combining human induced pluripotent stem cells (hiPSCs), bioengineered vascular grafts (BVGs), and gene editing. We generated BVGs from isogenic control hiPSC-derived vascular smooth muscle cells (SMCs) and mutant SMCs gene-edited to carry a Loeys-Dietz syndrome (LDS)–associated pathogenic variant (*TGFBR1*^{A230T}). We also generated hiPSC-derived BVGs using cells from a patient with LDS (*Patient*$^{A230T/+}$) and using genetically corrected cells (*Patient*$^{+/+}$). Control and experimental BVGs were then implanted into the common carotid arteries of nude rats. The *TGFBR1*^{A230T} variant led to impaired mechanical properties of BVGs, resulting in lower burst pressure and suture retention strength. BVGs carrying the variant dilated over time in vivo, resembling human TAA formation. Spatial transcriptomics profiling revealed defective expression of extracellular matrix (ECM) formation genes in *Patient*$^{A230T/+}$ BVGs compared with *Patient*$^{+/+}$ BVGs. Histological analysis and protein assays validated quantitative and qualitative ECM defects in *Patient*$^{A230T/+}$ BVGs and patient tissue, including decreased collagen hydroxylation. SMC organization was also impaired in *Patient*$^{A230T/+}$ BVGs as confirmed by vascular contraction testing. Silencing of collagen-modifying enzymes with small interfering RNAs reduced collagen proline hydroxylation in SMC-derived tissue constructs. These studies demonstrated the utility of BVGs to model human TAA formation in an animal host and highlighted the role of reduced collagen modifying enzyme activity in human TAA formation.

INTRODUCTION

Thoracic aortic aneurysm (TAA) is among the leading causes of death in the United States, with surgical repair as the only effective treatment (*1*–*4*). Animal models have been used to study TAA for years and have provided key insights into the developmental origins of aortic smooth muscle cells (SMCs) and aneurysm-related signaling events (*4*–*7*). However, these studies have not yielded a major therapeutic advance in preventing or reversing human TAAs. This cross-species discrepancy highlights the need for a more predictive human cell-based disease model to capture the human aneurysm pathogenesis (*8*, *9*). Human TAA studies have been limited to the examination of end-stage human aneurysmal tissue, which undergoes compensatory molecular and cellular changes during aneurysm progression. Lack of access to pre-aneurysmal human tissue from predisposed individuals further impedes our ability to discern early molecular events leading to TAA formation and further indicates the need to develop better disease models.

SMCs are the primary cell type that form the vascular wall and are essential to sustain arterial structure and function (*9*, *10*). In response to pathogenic conditions and vascular injury, SMCs can undergo marked phenotypic and functional changes (*10*–*14*). Aortic SMCs have heterogeneous developmental origins based on their spatial location, and several forms of aortic diseases, including aneurysm and atherosclerosis, show regional specificity. Recent fate mapping studies in animal models confirmed that regional TAA manifestations are attributable to the embryonic origins of SMCs (*9*, *15*–*18*). The integrity of the aortic wall relies on the interactions among SMCs, collagen, elastin, and other components of the extracellular matrix (ECM) (*6*). In addition, genes encoding collagen-modifying enzymes have also been implicated in aortic aneurysm, dissection, and rupture (*19*–*22*). However, compensatory changes in collagen quantity observed in some end-stage aneurysmal tissues complicate the interpretation of the role of collagen in TAA formation (*23*, *24*).

Genetic predisposition plays a more dominant role in TAA compared with abdominal aortic aneurysm (*6*, *13*). Pathogenic variants in genes involved in canonical transforming growth factor–β (TGF-β) signaling, including transforming growth factor–beta receptor type I (*TGFBR1*), cause Loeys-Dietz syndrome (LDS), a genetic disorder characterized by aortic root aneurysms (*6*, *25*). An LDS mouse model demonstrated that *Tgfbr1*$^{M318R/+}$ mutation disrupts SMCs derived from second heart field cardiovascular progenitor cells (CPCs) that are populated in the aortic root (*15*). In a previous study, we also identified a pathogenic *TGFBR1* variant (*TGFBR1*^{A230T}) causing aortic root aneurysm and aortic dissection in an LDS family (*26*). Our molecular characterization using human induced pluripotent stem cell (hiPSC) disease modeling revealed that *TGFBR1*^{A230T} impairs SMC gene expression and function in a lineage-specific manner, affecting cardiovascular progenitor cell lineage SMCs (CPC-SMCs) (*26*). Although the lineage-specific molecular and cellular defects informed the etiology of LDS-associated aortic root aneurysms, this previous study was largely limited to two-dimensional monolayer cell cultures lacking relevant environmental cues such as hemodynamic stress and intercellular SMC communication defined by vascular geometry (*26*). Therefore, the production of implantable three-dimensional tissue

[1]Department of Cardiac Surgery, University of Michigan, Ann Arbor, MI 48109, USA. [2]Second Xiangya Hospital, Central South University, Changsha, 410011, China. [3]Department of Internal Medicine, University of Michigan, Ann Arbor, MI 48109, USA.
*Corresponding author. Email: boya@med.umich.edu (B.Y.); dmizrak@med.umich.edu (D.M.); echenum@umich.edu (Y.E.C.)

constructs is necessary to make an improved human cell-based disease model (*8*).

To investigate the molecular events leading to human aneurysm formation, we developed a human TAA model in an animal host by combining hiPSCs, CRISPR-Cas9 gene editing, and bioengineered vascular grafts (BVGs). This platform enabled us to capture features of aortic root aneurysm formation associated with the *TGFBR1*^{A230T} variant. Here, we present evidence that collagen defects, likely caused by reduced collagen-modifying enzyme activity, contribute to the weaker mechanical performance of *TGFBR1*^{A230T} BVGs in vivo and lead to BVG dilation.

RESULTS

TGFBR1^{A230T} mutation impairs the mechanical properties of SMC-derived BVGs

To model aortic root aneurysm associated with the *TGFBR1*^{A230T} mutation, we generated implantable BVGs using isogenic male *TGFBR1*$^{+/+}$ (derived from a patient with no aortic abnormalities and denoted as control-I) and *TGFBR1*$^{A230T/+}$ hiPSCs (Fig. 1A and fig. S1A). To generate the BVGs, we modified previously published protocols (*27*, *28*). Briefly, instead of SMCs derived from embryoid bodies, we used maturation medium–treated CPC-SMCs (M-SMCs) with enhanced myosin heavy chain 11 (*MYH11*) expression (fig. S1B). We seeded M-SMCs derived from *TGFBR1*$^{+/+}$ and *TGFBR1*$^{A230T/+}$ hiPSCs onto polyglycolide [polyglycolic acid (PGA)] mesh and cultured them in petri dishes in vitro (fig. S1C), which resulted in vessel-like BVGs after 8 weeks (fig. S1D). Both *TGFBR1*$^{+/+}$ and *TGFBR1*$^{A230T/+}$ BVGs appeared opaque at the end of the in vitro culture period (Fig. 1B). Next, we characterized the mechanical properties of *TGFBR1*$^{+/+}$ and *TGFBR1*$^{A230T/+}$ BVGs using burst pressure, suture retention strength, and tensile tests. The *TGFBR1*$^{+/+}$ BVGs demonstrated a burst pressure of 2324 ± 211 mmHg, comparable to that of the saphenous vein (*29*). However, the BVGs generated from two independent *TGFBR1*$^{A230T/+}$ clones displayed significantly lower burst pressure (1385 ± 147 mmHg, 1300 ± 165 mmHg; $P < 0.001$) (Fig. 1C). Their suture retention strength was also significantly lower (0.86 ± 0.08 MPa, 0.83 ± 0.09 MPa; $P < 0.001$) compared with that of the isogenic *TGFBR1*$^{+/+}$ BVGs (1.31 ± 0.14 MPa) (Fig. 1D). In addition, we measured ultimate tensile stress of the BVGs by stretching tissue rings with custom rectangular loops and generated stress-strain plots. We observed lower ultimate tensile stress of *TGFBR1*$^{A230T/+}$ BVGs (0.70 ± 0.07 MPa, 0.66 ± 0.07 MPa) compared with their isogenic control BVGs (1.34 ± 0.14 MPa) and similar failure strain for both conditions (Fig. 1, E and F).

To verify that *TGFBR1*^{A230T} BVG mechanical defects were independent of genetic background, we used CRISPR-Cas9 gene editing to generate *TGFBR1*$^{A230T/+}$ lines using a different hiPSC control derived from a male participant with no aortic abnormalities (fig. S1E). We then generated BVGs from both isogenic control (denoted as control-II) and mutant cells (Fig. 1G) and measured their mechanical properties. Consistently, *TGFBR1*$^{A230T/+}$ BVGs generated from two independent clones (denoted as clone A and clone B) had weaker mechanical properties with lower burst pressure (*TGFBR1*$^{A230T/+}$ clone A: 861 ± 181 mmHg; *TGFBR1*$^{A230T/+}$ clone B: 895 ± 184 mmHg), suture retention strength (*TGFBR1*$^{A230T/+}$ clone A: 0.51 ± 0.09 MPa; *TGFBR1*$^{A230T/+}$ clone B: 0.51 ± 0.14 MPa), and ultimate tensile stress (*TGFBR1*$^{A230T/+}$ clone A: 0.47 ± 0.09 MPa; *TGFBR1*$^{A230T/+}$ clone B: 0.48 ± 0.10 MPa) values compared with their isogenic control (burst pressure: 1712 ± 183 mmHg; suture retention strength 0.90 ± 0.09 MPa; ultimate tensile stress 0.80 ± 0.07 MPa) (Fig. 1, H to J). Reduction in mechanical performance of the *TGFBR1*^{A230T} BVGs was consistent between independent hiPSC lines and clones confirming the pervasiveness of the mutation. Overall, these results demonstrated our ability to generate implantable BVGs and confirmed that the *TGFBR1*^{A230T} mutation impairs BVG mechanical properties in vitro.

A human aneurysm model is established in vivo using BVGs carrying the *TGFBR1*$^{A230T/+}$ mutation

To compare the in vivo performance of each BVG pair, we replaced one common carotid artery with *TGFBR1*$^{+/+}$ BVG and the other common carotid artery with *TGFBR1*$^{A230T/+}$ BVG in the same 3- to 4-month-old *Foxn1*^{RNU} nude rat using an optimized cuff technique (Fig. 2A) (*30*, *31*). The cuff served as a physical barrier between the host vessel and the BVG to reduce host cell migration onto the BVGs. We randomized the implantation side of *TGFBR1*$^{+/+}$ and *TGFBR1*$^{A230T/+}$ BVGs to control for the possibility of any left-right hemodynamic asymmetry in common carotid arteries that might affect the performance of the BVG (*32*). The animals received daily intraperitoneal enoxaparin injections to prevent thrombosis. Patent blood flow in both *TGFBR1*$^{+/+}$ and *TGFBR1*$^{A230T/+}$ BVGs after placement was confirmed by Doppler imaging (fig. S2A). The explanted *TGFBR1*$^{+/+}$ and *TGFBR1*$^{A230T/+}$ BVGs were patent with no signs of rupture or teratoma at week 8 after operation (fig. S2B). These results suggested that common carotid arteries of nude rats could support bilateral BVG implants and that both *TGFBR1*$^{+/+}$ and *TGFBR1*$^{A230T/+}$ BVGs were able to withstand the blood pressure during this 8-week period (fig. S2B).

After implantation, the in vivo patency and mid-vessel inner diameter change of the implanted BVGs were monitored by biweekly ultrasonography for 8 weeks. The cross-section ultrasound images revealed a visible inner diameter difference between *TGFBR1*$^{+/+}$ and *TGFBR1*$^{A230T/+}$ BVGs at week 8, although they appeared similar at week 1 (Fig. 2B). The inner diameter of *TGFBR1*$^{A230T/+}$ BVGs gradually increased over time, with a nearly 30% dilation by week 8 (Fig. 2, C and D; $n = 6$ biological replicates). The quantification of the biweekly ultrasound images showed significant *TGFBR1*$^{A230T/+}$ BVG dilation by week 8 compared with the isogenic *TGFBR1*$^{+/+}$ BVGs ($P < 0.01$; Fig. 2C and figs. S3 and S4; $n = 6$ biological replicates). The quantifications were performed on five pairs of bilaterally implanted BVGs and two unilateral BVGs. The inner diameters of pre-implantation BVGs (week 0) were measured using a vernier caliper. *TGFBR1*$^{+/+}$ BVGs slightly dilated by week 8, suggesting that control BVGs underwent remodeling to adapt to the in vivo factors including hemodynamic stress. However, *TGFBR1*$^{A230T/+}$ BVGs continued to dilate significantly after 4 weeks ($P < 0.05$; Fig. 2D). These results suggested that the *TGFBR1*^{A230T} mutation altered the ability of BVGs to withstand the strain from blood flow in nude rats leading to vessel dilation.

Patient$^{A230T/+}$ BVGs form dilation in vivo compared with genetically corrected *Patient*$^{+/+}$ BVGs

To confirm the in vivo dilation phenotype in patient-derived hiPSCs, we generated BVGs from a patient with LDS (*Patient*$^{A230T/+}$) and genetically corrected (denoted as *Patient*$^{+/+}$) cells (Fig. 3A). Both *Patient*$^{A230T/+}$ and *Patient*$^{+/+}$ hiPSC-derived CPC-SMCs formed opaque BVGs (Fig. 3B). In vitro mechanical tests revealed that the *Patient*$^{+/+}$ BVGs displayed a significantly higher burst pressure ($P < 0.001$; 1414 ± 122 mmHg) compared with *Patient*$^{A230T/+}$ BVGs (758 ± 86 mmHg),

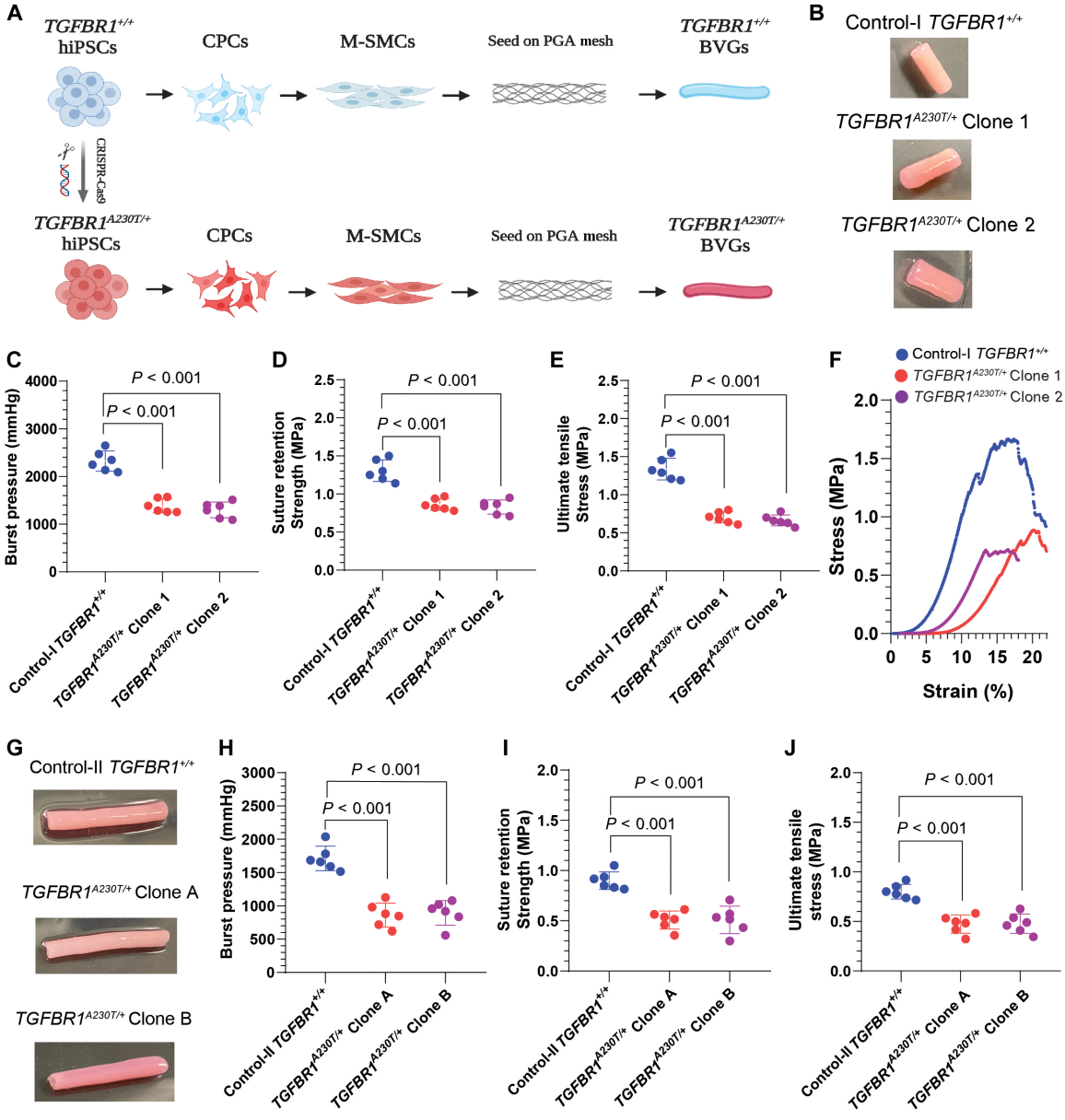

Fig. 1. *TGFBR1*^{A230T} mutation impairs the mechanical properties of SMC-derived BVGs in vitro. (**A**) Schematic illustration of BVG generation using hiPSC-derived SMCs through CPC lineage. *TGFBR1*$^{+/+}$ and *TGFBR1*$^{A230T/+}$ M-SMCs were seeded onto biodegradable PGA-based mesh and cultured for 8 weeks in vitro. Created with BioRender.com. (**B**) Representative images of BVGs derived from isogenic control-I *TGFBR1*$^{+/+}$ and *TGFBR1*$^{A230T/+}$ (two independent clones) SMCs after 8 weeks of in vitro culture. The mechanical properties including burst pressure (**C**), suture retention strength (**D**), and ultimate tensile stress (**E**) of *TGFBR1*$^{+/+}$ and *TGFBR1*$^{A230T/+}$ BVGs were measured (one-way ANOVA with Tukey's multiple comparisons test; $n = 6$ biological replicates). (**F**) Representative stress-strain plots from *TGFBR1*$^{+/+}$ and *TGFBR1*$^{A230T/+}$ BVGs. (**G**) Representative images of BVGs generated from isogenic control-II *TGFBR1*$^{+/+}$ and *TGFBR1*$^{A230T/+}$ (two independent clones) CPC-SMCs after 8 weeks of in vitro culture. The mechanical properties including burst pressure (**H**), suture retention strength (**I**), and ultimate tensile stress (**J**) of control-II *TGFBR1*$^{+/+}$ and *TGFBR1*$^{A230T/+}$ BVGs were measured (one-way ANOVA with Tukey's multiple comparisons test; $n = 6$ biological replicates).

with a nearly 80% increase (Fig. 3C). Consistently, the suture retention strength and ultimate tensile stress of the *Patient*$^{+/+}$ BVGs (0.92 ± 0.07 MPa and 0.82 ± 0.05 MPa) were enhanced compared with the *Patient*$^{A230T/+}$ BVGs (0.50 ± 0.07 MPa and 0.48 ± 0.05 MPa) (Fig. 3, D and E). The improved mechanical performance of *Patient*$^{+/+}$ BVGs was further demonstrated with the stress-strain test (Fig. 3F). These results were consistent with the in vitro mechanical differences between *TGFBR1*$^{+/+}$ and *TGFBR1*$^{A230T/+}$ BVGs.

We next measured cell density, remaining PGA amount, and BVG thickness at multiple time points to better understand the in vitro mechanical differences between the *Patient*$^{A230T/+}$ and *Patient*$^{+/+}$ BVGs. The BVG thickness remained the same during the BVG generation (fig. S5A). We observed a gradual increase in cell density and a gradual decrease in the PGA amount by week 8 of BVG generation in both *Patient*$^{A230T/+}$ and *Patient*$^{+/+}$ BVGs, with no differences between the groups (fig. S5, B and C). To assess the ECM deposition, we

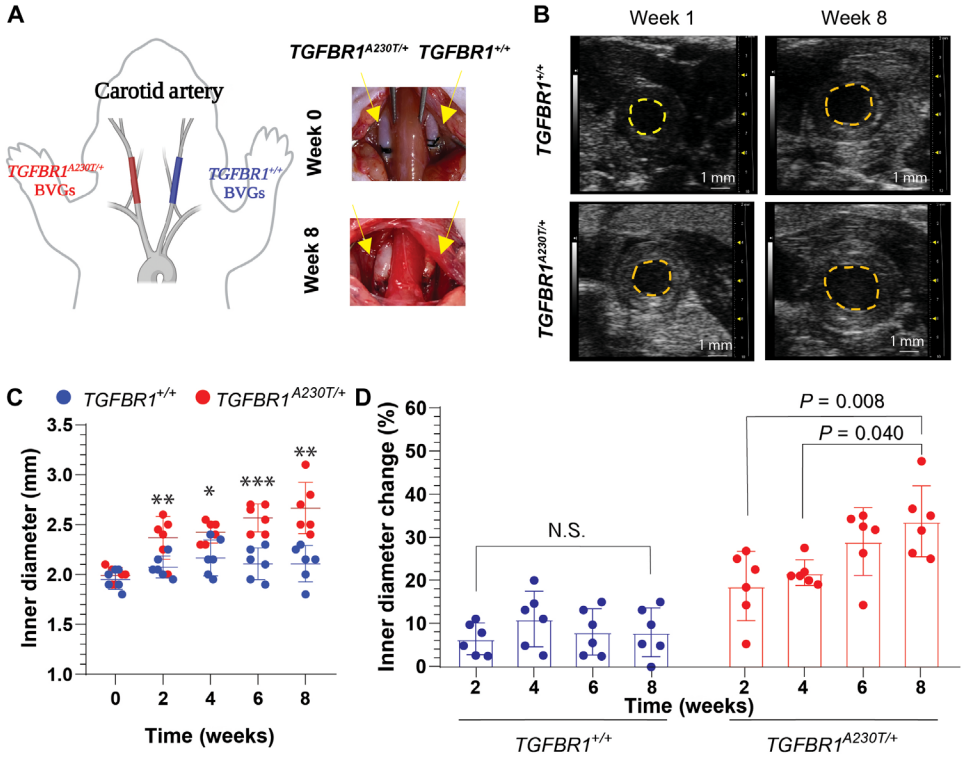

Fig. 2. Establishing an in vivo human aneurysm disease model using *TGFBR1*$^{A230T/+}$ BVGs implanted into nude rats. (**A**) Left: Schematic illustration of the disease model established by BVG implantation into the common carotid arteries of nude rats using an optimized cuff technique. Created with BioRender.com. Right: Representative images of implanted *TGFBR1*$^{+/+}$ and *TGFBR1*$^{A230T/+}$ BVGs in nude rats at week 0 and week 8 post-operation. (**B**) Representative ultrasound cross-section images, showing the inner diameters of *TGFBR1*$^{+/+}$ and *TGFBR1*$^{A230T/+}$ BVGs at week 1 and week 8. The inner diameters (**C**) and the inner diameter change (unpaired t test; $n = 6$ biological replicates; $^{*}P < 0.05$, $^{**}P < 0.01$, and $^{***}P < 0.001$) (**D**) of the implanted *TGFBR1*$^{+/+}$ and *TGFBR1*$^{A230T/+}$ BVGs were monitored for 8 weeks by ultrasonography (one-way ANOVA with Tukey's multiple comparisons test; $n = 6$ biological replicates). N.S., not significant.

performed a colorimetric hydroxyproline assay as a proxy to quantify collagen amount. Hydroxyproline content gradually increased in both groups over time; however, hydroxyproline content was significantly increased in *Patient*$^{+/+}$ BVGs compared with *Patient*$^{A230T/+}$ BVGs at 6 and 8 weeks (week 6, $P = 0.032$; week 8, $P = 0.035$; fig. S5D).

Patient$^{A230T/+}$ and *Patient*$^{+/+}$ BVGs were then implanted into the common carotid arteries of the nude rats, with the implantation side of the *Patient*$^{A230T/+}$ and *Patient*$^{+/+}$ BVGs randomized as described above ($n = 6$ biological replicates). The in vivo patency and inner diameter change were monitored by biweekly ultrasonography, which confirmed patent blood flow in both BVG groups (fig. S5E). The harvested *Patient*$^{A230T/+}$ BVGs showed dilation along the vessel at week 8 (Fig. 3G). Ultrasound cross-section images also demonstrated dilation by week 8 after operation (Fig. 3H). The inner diameters of pre-implantation BVGs (week 0) were measured using a vernier caliper. The quantification of inner dimeter change over time displayed a gradual inner diameter increase in *Patient*$^{A230T/+}$ BVGs from an average of 1.94 mm at week 0 to 2.73 mm by week 8, a nearly 40% increase (Fig. 3, I and J, and figs. S6 and S7). The quantifications were performed on four pairs of bilaterally implanted BVGs and four unilateral BVGs. The *Patient*$^{+/+}$ BVGs did not dilate in vivo, whereas the inner diameters of *Patient*$^{A230T/+}$ BVGs showed a significant increase from week 2 to week 4 ($P = 0.023$) and continued to dilate up to week 8 ($P < 0.001$; Fig. 3J).

To begin to characterize the cell types in the BVGs, we first performed HLA-A (human leukocyte antigens) staining to quantify host cell invasion on both *Patient*$^{A230T/+}$ and *Patient*$^{+/+}$ BVGs over time. The majority of BVG cells at week 8 were of human origin (HLA-A^{+}) (fig. S8, A and B). We also performed CD68 staining on the explanted BVGs to label monocyte lineage cells, particularly circulating macrophages (*33*). We detected CD68^{+} cells in both conditions, suggesting host immune cell infiltration by week 8 after operation (fig. S8C). CD68^{+} cells were significantly higher in *Patient*$^{A230T/+}$ BVGs ($P = 0.04$; fig. S8D), consistent with the finding that TAAs often present with inflammatory cells in the aortic wall media (*34*).

Spatial transcriptomics profiling reveals the molecular defects in *Patient*$^{A230T/+}$ BVGs

To elucidate the molecular mechanisms underlying the dilation that occurred in *Patient*$^{A230T/+}$ BVGs, we performed spatial transcriptomics profiling of two biological replicates of *Patient*$^{A230T/+}$ and *Patient*$^{+/+}$ BVGs explanted at week 8 after placement. To do this, the explanted BVGs were fixed in 4% paraformaldehyde solution and embedded in paraffin. Formalin-fixed, paraffin-embedded (FFPE; 5-μm thick) sections for each condition were placed on 10X Visium Spatial Gene Expression slides. The Visium FFPE probes targeting human genes revealed the gene expression patterns in each spatially barcoded spot (55 μm in diameter), which encompassed multiple cells capturing thousands of genes per sample (fig. S9A). We performed dimensionality reduction and unsupervised clustering using Seurat 4.2 (R package) to identify spatially resolved clusters and their distribution in two biological replicates of *Patient*$^{A230T/+}$ and *Patient*$^{+/+}$ BVGs (Fig. 4A) (*35*). We identified several clusters (denoted C1 to C7) with different gene expression patterns (data file S1). C1, C6, and C7 had overlapping marker expression with variable expressivity including the enrichment of potassium calcium-activated channel subfamily M alpha 1 (*KCNMA1*); therefore, they were colored similarly in different shades of red (Fig. 4A).

The resulting clusters exhibited differential distribution among the *Patient*$^{A230T/+}$ and *Patient*$^{+/+}$ BVGs (Fig. 4B and fig. S9B). C1 and C5 were more prevalent in the *Patient*$^{A230T/+}$ BVGs (Fig. 4B). C2, enriched

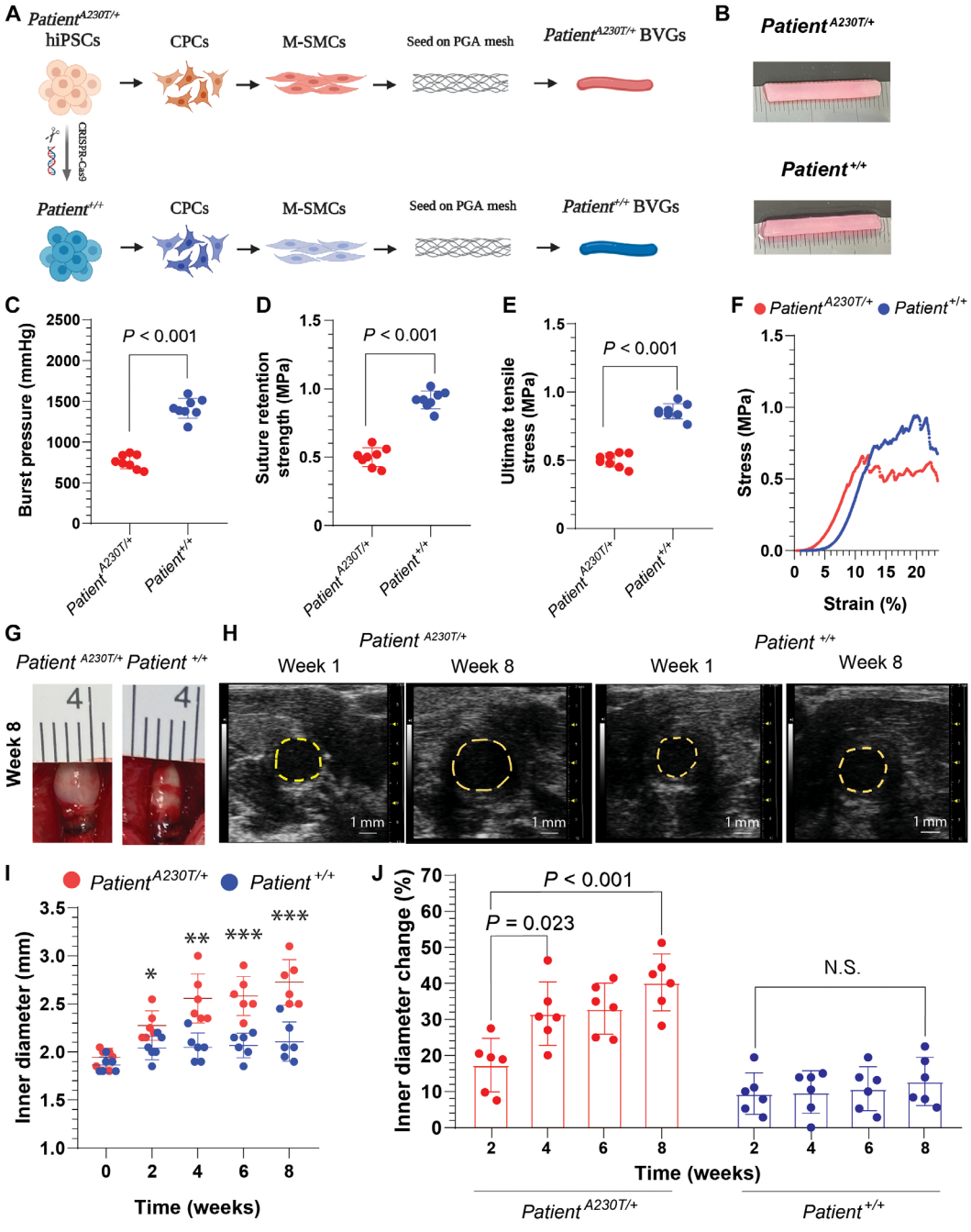

Fig. 3. *Patient*$^{A230T/+}$ BVGs have weaker mechanical performance in vitro and dilate over 8 weeks in vivo. (**A**) Schematic illustration of BVG generation using *Patient*$^{A230T/+}$ and patient-corrected *Patient*$^{+/+}$ hiPSC-derived SMCs. M-SMCs were seeded onto PGA-based mesh and cultured for 8 weeks in vitro. Created with BioRender.com. (**B**) Representative images of BVGs from *Patient*$^{A230T/+}$ and *Patient*$^{+/+}$ hiPSC-derived SMCs after 8 weeks of in vitro culture. The mechanical properties including burst pressure (**C**), suture retention strength (**D**), and ultimate tensile stress (**E**) of *Patient*$^{A230T/+}$ and *Patient*$^{+/+}$ BVGs were measured (unpaired *t* test; $n = 8$ biological replicates). (**F**) Representative stress-strain plots from the *Patient*$^{A230T/+}$ and *Patient*$^{+/+}$ BVGs. (**G**) Representative images of the explanted *Patient*$^{A230T/+}$ and *Patient*$^{+/+}$ BVGs at week 8 post-operation. (**H**) Representative ultrasound images showing the inner diameters of *Patient*$^{A230T/+}$ and *Patient*$^{+/+}$ BVGs in nude rats at week 1 and week 8. (**I** and **J**) Inner diameters (unpaired t test; $n = 6$ biological replicates; $^{*}P < 0.05$, $^{**}P < 0.01$, and $^{***}P < 0.001$) and the inner diameter change of the implanted *Patient*$^{A230T/+}$ and *Patient*$^{+/+}$ BVGs (one-way ANOVA with Tukey's multiple comparisons test; $n = 6$ biological replicates) were monitored for 8 weeks by ultrasonography.

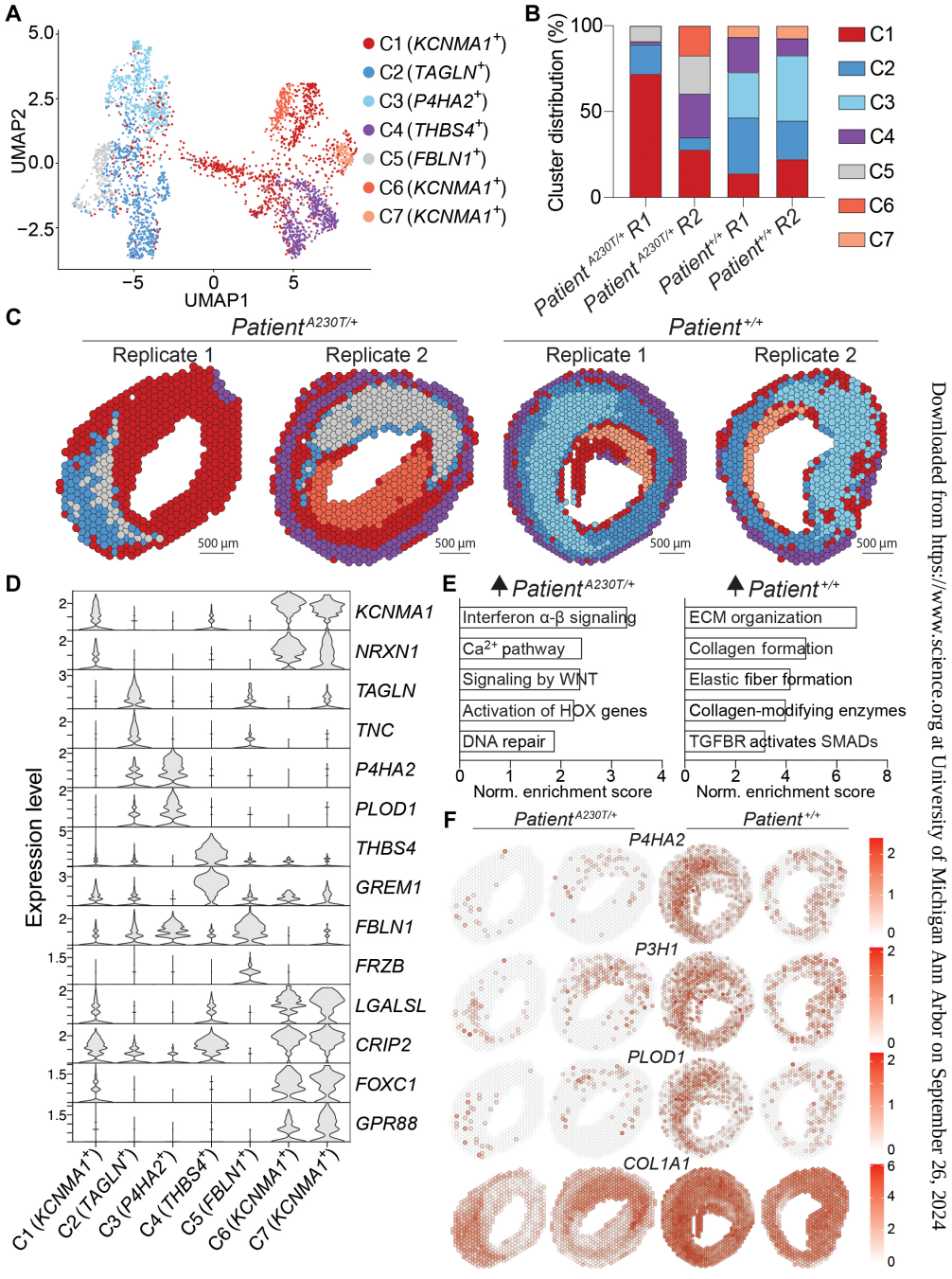

Fig. 4. Spatial transcriptomics profiling reveals ECM defects in *Patient* $^{A230T/+}$ BVGs. (**A**) Uniform Manifold Approximation and Projection (UMAP) visualization of different clusters (C1 to C7) in the merged spatial transcriptomics dataset. Related C1, C6, and C7 clusters are colored in different shades of red because they exhibited overlapping marker expression with variable expressivity. One of the top enriched genes is highlighted for each cluster. (**B**) Fraction of different clusters (C1 to C7) in each sample demonstrating their cluster composition. Two biological replicates of the *Patient*$^{A230T/+}$ and *Patient*$^{+/+}$ BVGs were analyzed. R1, replicate 1; R2, replicate 2. (**C**) Spatial distribution of different clusters in two replicates of *Patient*$^{A230T/+}$ and *Patient*$^{+/+}$ BVGs. Each circle corresponds to a barcoded spatial spot (55 μm in diameter), and the size of the spots was adjusted by Seurat to improve visualization. (**D**) Violin plots showing normalized expression of enriched cluster markers. (**E**) Gene set enrichment analysis using the Reactome Pathway Database showing the enrichment of different gene sets in *Patient*$^{A230T/+}$ versus *Patient*$^{+/+}$ comparison ranked by normalized (Norm.) enrichment score. (**F**) Spatially resolved normalized expression of *P4HA2*, *P3H1*, *PLOD1*, and *COL1A1* in two biological replicates of *Patient*$^{A230T/+}$ and *Patient*$^{+/+}$ BVGs.

in the SMC marker transgelin (*TAGLN*), and C3, enriched in collagen-modifying enzymes including prolyl 4-hydroxylase subunit alpha 2 (*P4HA2*) and lysyl hydroxylase 1 (*PLOD1*), were the most abundant clusters in the *Patient*$^{+/+}$ BVGs (Fig. 4B and data file S1). Thrombospondin 4 (*THBS4*)–enriched C4 cluster marked the outer layer of BVGs from both conditions (Fig. 4, C and D), and *THBS4* deficiency increases aortic dissection risk (*36*). *Patient*$^{A230T/+}$ BVG walls were mostly populated with C1, C6, and C5, enriched in the fibroblast marker fibulin 1 (*FBLN1*) (Fig. 4, C and D). SMC-related clusters, C2 and C3, formed the wall of *Patient*$^{+/+}$ BVGs but only labeled isolated regions in *Patient*$^{A230T/+}$ BVGs (Fig. 4C). Examination of additional cluster markers supported cell identity differences between *Patient*$^{A230T/+}$ and *Patient*$^{+/+}$ BVGs (data file S1 and fig. S9C).

Next, we performed differential gene expression analysis comparing the *Patient*$^{A230T/+}$ and *Patient*$^{+/+}$ BVGs using Seurat 4.2 (R package) (data file S1). *TGFBR1*^{A230T} variant impaired the expression of SMC contraction genes, including smoothelin (*SMTN*) and *TAGLN* in the *Patient*$^{A230T/+}$ BVGs (P-adjusted < 0.001; data file S1). Using gene set enrichment analysis, we also identified Reactome pathways up-regulated in each condition (Fig. 4E) (*37*). *Patient*$^{A230T/+}$ BVGs were enriched in injury- and repair-related gene sets, including interferon signaling and DNA repair (Fig. 4E). ECM organization,

collagen formation, collagen-modifying enzymes, and elastic fiber formation gene sets showed enrichment in the *Patient*$^{+/+}$ condition [false discovery rate (FDR) < 0.001; data file S1]. Consistently, several enzymes involved in the hydroxylation of proline and lysine residues on collagen—including *P4HA2*, prolyl 3-hydroxylase 1 (*P3H1*), *PLOD1*, *PLOD2*, and lysyl oxidase (*LOX*)—were significantly enriched in *Patient*$^{+/+}$ BVGs (*P*-adjusted < 0.001; data file S1). Increased TGF-β signaling in the *Patient*$^{+/+}$ BVGs compared with the *Patient*$^{A230T/+}$ BVGs supported the persistent effect of the *TGFBR1*^{A230T} variant in vivo (Fig. 4E). In addition, respiratory electron transport and citric acid cycle gene sets were enriched in the *Patient*$^{+/+}$ condition, suggesting enhanced mitochondrial function (FDR < 0.001; data file S1). To visualize collagen-related expression changes, we plotted spatial expression profiles of *P4HA2*, *P3H1*, *PLOD1*, and collagen type I alpha 1 chain (*COL1A1*), which revealed uneven distribution and lower expression of these markers in *Patient*$^{A230T/+}$ BVGs (Fig. 4F). Overall, these data suggested potential ECM defects underlying *Patient*$^{A230T/+}$ BVG dilation in vivo.

Orthogonal validations confirm ECM defects in explanted *Patient*$^{A230T/+}$ BVGs

To validate the ECM expression defects in the *Patient*$^{A230T/+}$ BVGs, we first assayed collagen quality in *Patient*$^{A230T/+}$ and *Patient*$^{+/+}$ BVGs before and after implantation. To distinguish thick and better aligned collagen fibers (shown in orange-red birefringence) from thin collagen fibers (green birefringence), we performed picrosirius red stainings enhanced with polarized light (Fig. 5A) (*38*, *39*). We did not detect differences in thick versus thin collagen fiber ratio between the pre-implantation *Patient*$^{A230T/+}$ and *Patient*$^{+/+}$ BVGs (Fig. 5, A and B). The explanted *Patient*$^{A230T/+}$ BVGs showed significantly lower thick/thin fiber ratio compared with the *Patient*$^{+/+}$ BVGs ($P = 0.006$; Fig. 5B and fig. S10A), suggesting qualitative collagen differences between the harvested *Patient*$^{A230T/+}$ and *Patient*$^{+/+}$ BVGs. To understand the pathological relevance of this finding, we performed picrosirius red stainings on aneurysmal root samples of patients from LDS families carrying *SMAD3* pathogenic variants and the LDS patient whose *Patient*$^{A230T/+}$ hiPSCs were modeled in Fig. 3 (Fig. 5C) (*40*). The collagen fibers appeared disorganized in the aneurysmal root samples with lower thick/thin collagen fiber ratio compared with the non-aneurysmal aortic roots (Fig. 5, C and D, and fig. S10B), supporting the findings in the BVGs.

Elastin is the major component of elastic fibers, fragmentation of which is a hallmark of human TAA (*41*). HiPSC-derived SMCs have very low elastin (*ELN*) expression in two-dimensional monolayer cultures, a major limitation of the hiPSC disease modeling (*42*). Next, we checked the spatial expression of several genes contributing to elastic fiber assembly (*13*, *43*, *44*), including fibrillin-1 (*FBN1*), fibulin-5 (*FBLN5*), and elastin microfibril interfacer 1 (*EMILIN1*) in *Patient*$^{A230T/+}$ and *Patient*$^{+/+}$ BVGs. *ELN*, *FBN1*, *FBLN5*, and *EMILIN1* were downregulated in *Patient*$^{A230T/+}$ BVGs (Fig. 5E). Immunohistochemical analysis also revealed significantly weaker ELN staining in the explanted *Patient*$^{A230T/+}$ BVGs compared with the *Patient*$^{+/+}$ BVGs ($P <$ 0.001; fig. S11A). The spatially resolved expression of these genes also showed regional overlap, indicating their coexpression in the same BVG areas (Fig. 5E). We then performed FBN1 and ELN costaining, which confirmed weaker FBN1 and ELN staining in *Patient*$^{A230T/+}$ BVGs and FBN1 and ELN colocalization in the BVGs (Fig. 5F). However, mature elastic fibers were not detected in either BVG condition, similar to previous studies involving hiPSC-SMC– or primary SMC-derived tissue-engineered vessel grafts (*28*, *45*, *46*). Overall, these data suggested that in vivo factors failed to promote the expression of key elastic fiber assembly genes in the *Patient*$^{A230T/+}$ BVGs; however, the conditions were also suboptimal for organized elastic fiber formation in the *Patient*$^{+/+}$ BVGs.

Patient$^{A230T/+}$ BVGs exhibit reduced collagen-modifying enzyme activity and vascular contractility

Next, we performed additional stainings and functional assays to further characterize the differences between *Patient*$^{A230T/+}$ and *Patient*$^{+/+}$ BVGs. MYH11^{+} SMCs were present in both *Patient*$^{A230T/+}$ and *Patient*$^{+/+}$ BVGs, and the top marker of C4, THBS4, labeled the outer layer of the BVGs from both conditions (Fig. 6A). We speculate that the THBS4^{+} cell population could also be important in adapting to the hemodynamic environment in vivo, given the known role of THBS4 in vascular remodeling (*36*). To examine how the changes in SMC contraction markers such as *TAGLN* translated into SMC function in the *Patient*$^{+/+}$ BVGs, we tested the vascular contraction of the BVGs using a myograph system (*47*). To accomplish this, BVG rings were prepared from both pre-implantation and explanted BVGs and were incubated in a myograph chamber. Contraction and relaxation of the BVG rings were induced using serotonin hydrochloride (5-HT) and sodium nitroprusside (SNP), respectively (Fig. 6B) (*47*–*49*). Consistent with the changes in SMC marker gene expression, vascular contraction was significantly impaired in the explanted *Patient*$^{A230T/+}$ BVGs, suggesting inferior SMC function and organization ($P = 0.017$; Fig. 6B). Vascular contractions were weak in both *Patient*$^{A230T/+}$ and *Patient*$^{+/+}$ pre-implantation BVGs, likely because of poor SMC alignment in vitro in the absence of hemodynamic cues (Fig. 6B).

We also further characterized collagen defects. First, human Pro-COL1A1 enzyme-linked immunosorbent assay (ELISA) on the explanted BVGs revealed significantly lower COL1A1 abundance in the *Patient*$^{A230T/+}$ BVGs ($P = 0.002$; Fig. 6C). We performed immunostainings for collagen-modifying enzymes, P4HA2 and PLOD1, which had stronger labeling in the explanted *Patient*$^{+/+}$ BVGs consistent with the gene expression differences (Fig. 6A and fig. S11, B and C). To measure the prolyl hydroxylase enzyme activity in the BVGs, we performed the hydroxyproline assay. Post-implantation BVGs appeared to have higher hydroxyproline content compared with the pre-implantation BVGs in both *Patient*$^{A230T/+}$ and *Patient*$^{+/+}$ BVGs, confirming ECM remodeling in vivo (Fig. 6D). Both pre-implantation and post-implantation *Patient*$^{A230T/+}$ BVGs had lower hydroxyproline content compared with the *Patient*$^{+/+}$ BVGs, suggesting impaired collagen modification in *Patient*$^{A230T/+}$ BVGs in vitro and in vivo (Fig. 6D).

To assess the functional effects of prolyl hydroxylases *P4HA2* and *P3H1* on CPC-SMC–derived collagen, we conducted gene silencing experiments using small interfering RNAs (siRNAs). We seeded *Patient*$^{A230T/+}$ and *Patient*$^{+/+}$ CPC-SMCs around agarose molds to allow them to form tissue rings, which have higher collagen content compared with two-dimensional cell cultures (*50*). We treated the tissue rings with nontargeting control siRNA pool or experimental siRNAs targeting either *P4HA2* or *P3H1* for 8 days (fig. S11D). Both *P4HA2* and *P3H1* siRNA-treated *Patient*$^{+/+}$ samples did not form strong tissue rings and had lower hydroxyproline content compared with the control ($P < 0.05$; Fig. 6E). Overall, these data suggested that reduced collagen quality and quantity may be attributed to impaired collagen-modifying enzyme activity in the *Patient*$^{A230T/+}$ BVGs and that these enzyme defects were a determinant of BVG performance in vivo.

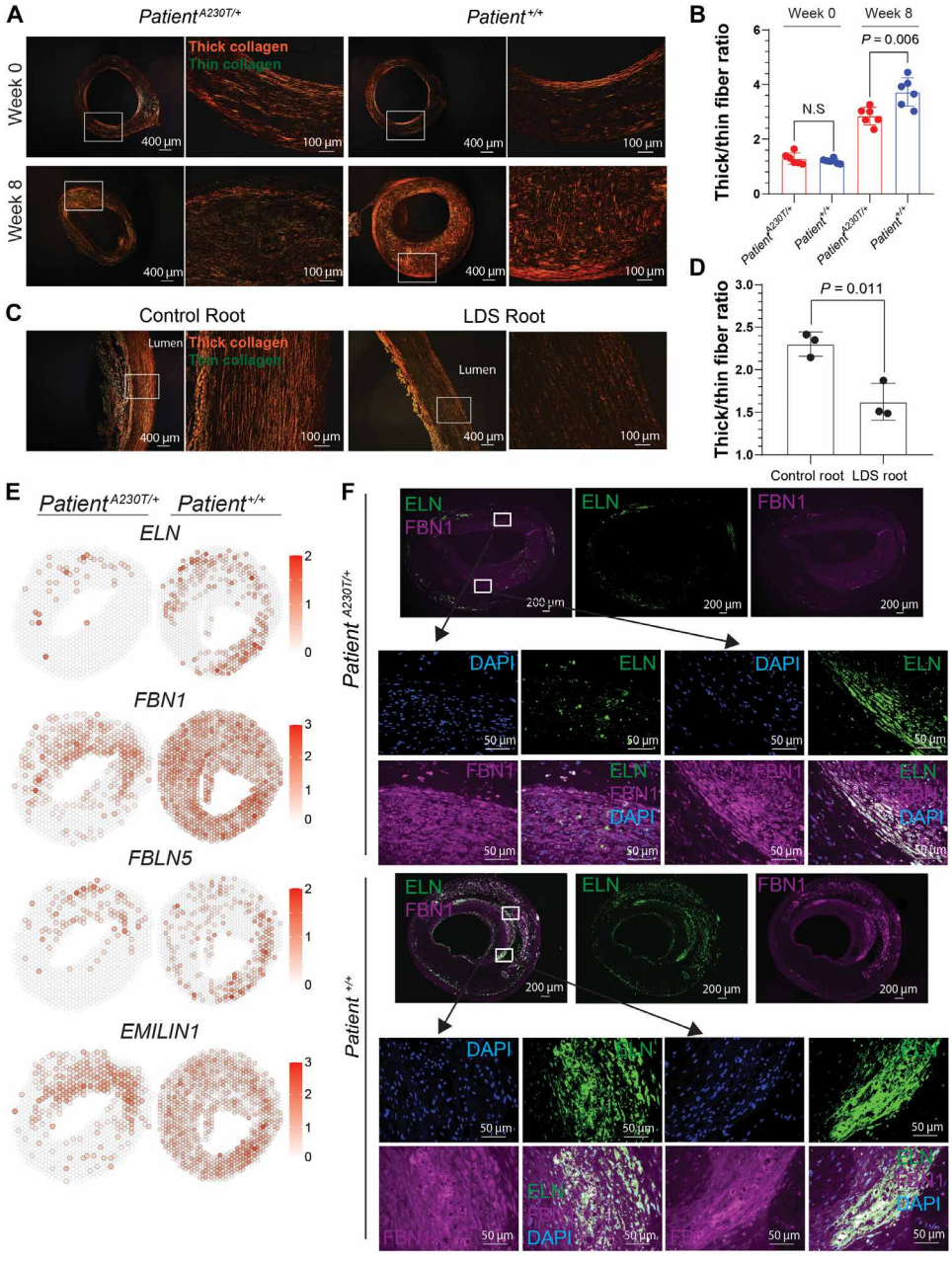

Fig. 5. Characterization of ECM defects in *Patient*$^{A230T/+}$ BVGs using histological analysis. (**A**) Picrosirius red stainings of pre-implantation (week 0, top) and explanted (week 8 after operation, bottom) *Patient*$^{A230T/+}$ and *Patient*$^{+/+}$ BVGs. The images were taken under a polarizing filter, where thick fibers are orange/red birefringence and thin fibers are green birefringence. (**B**) Quantification of the thick/thin fiber ratios of pre-implantation (week 0) and explanted (week 8) BVGs (unpaired *t* test; $n = 6$ biological replicates). (**C**) Representative picrosirius red stainings of aortic root samples from the patient carrying the *TGFBR1*^{A230T} variant and a control with no aortic abnormalities. (**D**) Quantification of the thick/thin fiber ratios of root samples from non-aneurysmal controls and patients from LDS families (unpaired *t* test; $n = 3$ biological replicates). (**E**) Spatially resolved expression of *ELN*, *FBN1*, *FBLN5*, and *EMILIN1* in the *Patient*$^{A230T/+}$ and *Patient*$^{+/+}$ BVGs. (**F**) Co-immunostainings for ELN (green) and FBN1 (purple) on *Patient*$^{A230T/+}$ and *Patient*$^{+/+}$ BVGs with 4′,6-diamidino-2-phenylindole (DAPI; blue) staining.

DISCUSSION

In this study, we developed a human aneurysm model by comparing hiPSC-derived BVGs carrying an LDS-associated *TGFBR1*^{A230T} mutation with their isogenic controls in nude rats. The *TGFBR1*^{A230T} mutation impaired the mechanical properties of both *Patient*$^{A230T/+}$ and *TGFBR1*$^{A230T/+}$ BVGs. This is consistent with our previous study that demonstrated reduced tensile strength in mutant tissue rings (*26*). Although the collagen fiber ratio was similar in the pre-implantation BVGs, we detected less thick collagen fiber in the explanted *Patient*$^{A230T/+}$ BVGs, suggesting that in vivo BVG remodeling was impaired by the *TGFBR1*^{A230T} mutation. Introduction of mechanical stretching by bioreactors increases the mechanical performance of tissue-engineered blood vessels and improves collagen synthesis (*28*, *46*, *51*, *52*). Thus, we speculate that mechanical stimulation from blood flow through the BVGs led to improved collagen synthesis and maturation as well as SMC alignment and function in the *Patient*$^{+/+}$ BVGs but that these processes were impeded in the *Patient*$^{A230T/+}$ BVGs, ultimately resulting in the gradual dilation of the *Patient*$^{A230T/+}$ BVGs.

The aortic root is mostly populated with CPC-SMCs, which have been associated with aortic root aneurysm formation in animal model studies (*9*, *15*). Our previous study also demonstrated that *TGFBR1*^{A230T} mutation impairs contractile gene expression and function in CPC-SMCs, sparing neural crest stem cell–derived SMCs, that populate the ascending aorta (*26*). In this study, we observed that vascular contraction was impaired in the explanted *Patient*$^{A230T/+}$ BVGs,

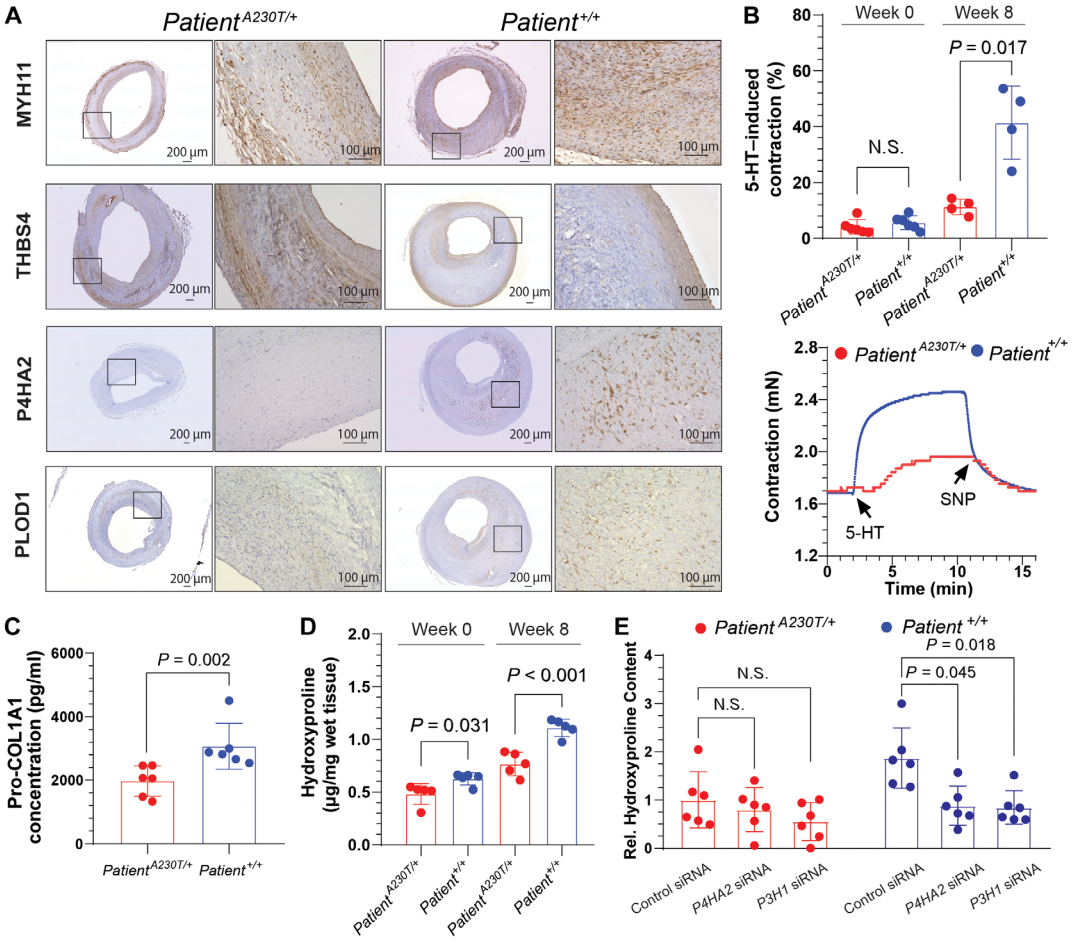

Fig. 6. *Patient*$^{A230T/+}$ BVGs display reduced collagen-modifying enzyme activity and vascular contractility. (**A**) Immunostainings for MYH11, THBS4, P4HA2, and PLOD1 in explanted *Patient*$^{A230T/+}$ and *Patient*$^{+/+}$ BVGs at week 8 after placement. (**B**) Top: Contraction change in pre-implantation (week 0; $n = 6$ biological replicates; Mann-Whitney test) and explanted BVGs (week 8 post-operation; $n = 4$ biological replicates; unpaired *t* test with Welch's correction). Bottom: A representative plot showing vascular contraction and relaxation of explanted BVGs in response to 5-HT and SNP, respectively. (**C**) Pro-COL1A1 quantification of explanted *Patient*$^{A230T/+}$ and *Patient*$^{+/+}$ BVGs (Mann-Whitney test; $n = 6$ biological replicates). (**D**) Hydroxyproline quantifications of the pre-implantation (week 0; $n = 5$ biological replicates; Mann-Whitney test) and explanted (week 8; $n = 5$ biological replicates; unpaired *t* test) *Patient*$^{A230T/+}$ and *Patient*$^{+/+}$ BVGs. (**E**) Relative hydroxyproline content of *Patient*$^{A230T/+}$ and *Patient*$^{+/+}$ tissue rings treated with nontargeting (control siRNA), *P4HA2*, or *P3H1* siRNA (*Patient*$^{A230T/+}$ comparison: one-way ANOVA with Tukey's multiple comparisons test; $n = 6$ biological replicates; *Patient*$^{+/+}$ comparison: Kruskal-Wallis test with Dunn's multiple comparisons test; $n = 6$ biological replicates). The average *Patient*$^{A230T/+}$ value treated with control siRNA was set to 1.

and gene expression data suggested mitochondrial dysfunction in *Patient*$^{A230T/+}$ BVGs. Reduced mitochondrial respiration was previously reported in *Tgfbr1*$^{M318R/+}$ SMCs, patient-derived fibroblasts carrying pathogenic variants in *TGFBR2* or *SMAD3*, *Fbn1*$^{c1039g/+}$ Marfan syndrome (MFS) mouse model, as well as aortic biopsies from patients with MFS (*53*–*55*). Mitochondrial decline may play a role in the functional SMC defects observed in *Patient*$^{A230T/+}$ BVGs. Vascular contraction derangements could impair the ability to adapt to the hemodynamic environment in vivo and contribute to vessel dilation and potentially rupture (*56*).

TGF-β signaling regulates SMC differentiation and vascular homeostasis as well as ECM remodeling by regulating collagen synthesis (*15*, *57*–*61*). SMAD3 is a key downstream effector of TGF-β signaling, and its deficiency reduced thick collagen fiber (collagen type I) abundance in aortic walls in a mouse model (*62*), consistent with these findings. Collagen type I provides structural support to ECM, conferring tensile strength, and its degradation is linked to connective tissue fragility in patients with aortopathies (*63*, *64*). Furthermore, *Col1a1*$^{\Delta/\Delta}$ mice have a substantially higher risk of aortic dissection and rupture, suggesting that the integrity of the aortic wall depends on adequate type I collagen content (*65*). Likewise, *COL3A1* mutations can cause vascular Ehlers-Danlos syndrome (vEDS). vEDS is characterized by fragile aortic walls leading to sudden thoracic descending aortic rupture that is usually not preceded by aortic dilatation (*66*–*68*). Nonaneurysmal descending aortic rupture is also reported in some MFS after previous prophylactic aortic root and ascending aorta repair (*69*). Among the elastic fiber formation genes tested, *FBN1* encodes a primary component of the microfibril scaffold and is the causative gene for MFS, an inherited disorder causing aortic root complications (*44*). In addition to its canonical role in elastic fiber assembly, FBN1 can also form an independent network with collagen. Mutations in *ELN* rarely cause aortic rupture, implicating the involvement of collagen

derangements in *FBN1*-associated aortopathies (*70*–*72*). In addition to our data showing a link between TGF-β signaling and ECM regulation, phenotypic characteristics of LDS, MFS, and vEDS imply a common signature of collagen defects underlying regional manifestations of TAA, dissection, and rupture as well as the distinct contributions of collagen subtypes to disease severity and susceptibility.

We also detected lower expression of collagen modifying lysyl and prolyl hydroxylase enzymes including *P4HA2*, *P3H1*, and *PLOD1* in *Patient*$^{A230T/+}$ BVGs compared with the *Patient*$^{+/+}$ group, and a hydroxyproline assay confirmed impaired prolyl hydroxylase enzyme activity in the *Patient*$^{A230T/+}$ BVGs. *PLOD1* catalyzes the hydroxylation of lysine residues on collagen, and aortas from *Plod1*$^{-/-}$ mice show degenerated collagen fibrils leading to aortic rupture (*19*, *20*). Pathogenic variants in *PLOD1* are associated with the kyphoscoliotic type of EDS typically characterized by hyperextensible skin and joint tissue (*73*, *74*). Several studies have identified inactivating *PLOD1* variants in families with TAA and dissection (*75*, *76*). Similarly, prolyl hydroxylase enzymes, including *P3H1* and *P4HA2,* catalyzing the hydroxylation of proline residues are critical for collagen triple helix formation and fiber stability. Prolyl hydroxylase deficiency can cause osteogenesis imperfecta, which is also associated with aortic root dilatation (*21*, *22*). A recent report also recommended cardiovascular screening for patients with osteogenesis imperfecta (*77*). Collagen-modifying enzymes are not limited to collagen hydroxylases. ADAMs family metalloproteinases have also been implicated in aortic aneurysm formation (*78*, *79*). Among the dysregulated metalloproteinases in *Patient*$^{A230T/+}$ BVGs, ADAM metallopeptidase with thrombospondin type 1 motif 2 (*ADAMTS2*) is a procollagen N-propeptidase promoting collagen fiber assembly and is implicated in EDS (*80*). These results support a role for collagen-modifying enzyme defects in aortic root aneurysms associated with impaired TGF-β signaling.

This study does have several limitations. To establish a disease model, we produced BVGs under static conditions. We acknowledge that BVGs generated with pulsatile stress have better mechanical performance (*28*, *46*, *51*, *52*). However, our *TGFBR1*$^{+/+}$ BVGs demonstrated high burst pressures, which we attribute to a higher CPC-SMC proliferation capacity and an optimized CPC-SMC maturation process. In addition, the PGA material was not fully degraded in the pre-implantation BVGs consistent with previous reports (*81*); however, the remaining material amount was not different between *Patient*$^{A230T/+}$ and *Patient*$^{+/+}$ BVGs. We used BVGs for the purpose of generating a human aortic aneurysm model, and we acknowledge that there are more sophisticated approaches for off-the-shelf BVG production (*27*, *28*, *82*). In addition, although we used a modified dual-cuff technique instead of suture anastomosis to decrease the direct contact between BVGs and host vessel, we still observed substantial host cell accumulation by week 8, affecting our ability to monitor aneurysm features for longer periods of time. Our BVGs also lacked organized elastic fibers, which is a fairly common issue in tissue-engineered blood vessel studies (*27*, *28*, *46*). Numerous strategies have been developed to improve tropoelastin and mature elastin expression in BVGs with limited success, indicating the need to understand the molecular basis of *ELN* expression and mature elastic fiber formation (*83*–*87*).

Despite these challenges, this BVG-based human aortic aneurysm model has the potential to provide insights into the early molecular events leading to TAA formation. By modeling LDS-associated aortic root aneurysms, we observed a convergence of TGF-β signaling defects and ECM deficiencies paralleling those found in other syndromes, such as MFS, EDS, and osteogenesis imperfecta. ECM network defects could be a key driver of TAA formation by compromising aortic wall integrity and disrupting mechanotransduction, leading to SMC dysfunction.

MATERIALS AND METHODS

Study design

The objective of this study was to establish a human aneurysm model by using BVGs carrying a LDS-associated pathogenic variant *TGFBR1*^{A230T} to mimic human TAA formation. We compared knock-in hiPSC-derived CPC-SMCs carrying the *TGFBR1*^{A230T} mutation with their isogenic controls and *Patient*$^{A230T/+}$ CPC-SMCs with patient-corrected cells (*Patient*$^{+/+}$). Mechanical studies including burst pressure and suture retention strength were performed on the BVGs in vitro. An in vivo human aneurysm model was established by implanting control and experimental BVGs into the common carotid arteries of nude rats. The inner diameter change of the BVGs was monitored using ultrasonography. The BVGs were harvested at week 8 after placement, and spatial transcriptomics profiling was performed to investigate the molecular and cellular defects. The findings were validated by quantitative and qualitative assays in BVGs and human aortic root samples. The experiments were performed according to the protocols approved by the Institutional Review Board at the University of Michigan (HUM00096079 and HUM00054585). All animal experiments were performed under the protocols approved by the Institutional Animal Care & Use Committee (PRO00011590) of the University of Michigan according to the National Institutes of Health guidelines, in collaboration with Unit for Laboratory Animal Medicine of University of Michigan. Detailed descriptions of additional experimental procedures and materials are available in Supplementary Materials and Methods and tables S1 to S3. Individual-level data for the main and supplementary figure column plots are included in data file S2. Detailed numbers of biological replicates are listed in the figure legends and data analysis sections to demonstrate biological reproducibility. We did not use statistical analysis to predetermine sample sizes. Animal enrollments to different groups were randomized. The ultrasound analyses were blinded, and all biweekly ultrasound data were included in the quantifications. We also included additional BVGs for molecular and cellular analyses, such as histological evaluations and vascular contraction assay and colored Doppler images, that were not monitored by biweekly ultrasonography.

hiPSC generation, and CRISPR-Cas9 gene editing

The hiPSCs were generated as described previously (*26*). *TGFBR1* was targeted using CRISPR-Cas9 gene editing. The *TGFBR1*$^{A230T/+}$ lines from control-I hiPSCs were generated previously (*26*). The *TGFBR1*$^{A230T/+}$ line using a different male hiPSC control (generated from a 41-year-old male with no aortic abnormalities), denoted as control-II, was generated as follows. Single guide RNA [sgRNA; obtained from Integrated DNA Technologies (IDT)] with the sequence 5′-CCACGAACGTTCTTCTCTAG-3′ was used to target the adjacent downstream of TGFBR1 c.688G. Two single-stranded oligodeoxynucleotides (ssODNs) (obtained from IDT) were designed to induce the *TGFBR1 c.688G > A* (p.Ala230Thr) mutation and *TGFBR1 c.688A>G* (p.Thr230Ala) correction by homology directed repair. To form the RNP complex, 10 μg (60 pmol) of S.p. HiFi Cas9 nuclease V3 (obtained from IDT) and 210 pmol of sgRNA were first incubated together for 10 min at room temperature. Two million hiPSCs were

electroporated with the RNP mixture using Celetrix electroporation system (Celetrix) with the following program: V set (630 V), T set (30 ms), P num (1 N), and P int (1 ms). Transfected hiPSCs were seeded on Corning GFR Matrigel-coated 60-mm dishes in TesRE8 medium (STEMCELL Technologies, catalog no. 05990) and cultured until visible clones were formed. Two heterozygous clones with the *TGFBR1* c. G688A mutation were selected for further experiments. ssODNs without the mutation were used to correct the *TGFBR1* gene in hiPSCs derived from patients with LDS. All generated clones were confirmed by Sanger sequencing.

Generation of BVGs

To generate BVGs, we differentiated hiPSCs to CPC-SMCs. For CPC-SMC differentiation, CPCs were digested by Accutase, centrifuged, and seeded with the density of 1.5×10^4 cells/cm^2 in CPC-SMC medium [Dulbecco's modified Eagle's medium (DMEM)/F12, B27, 1% penicillin-streptomycin, 1-thioglycerol (400 μmol/liter), TGF-β1 (2 ng/ml), and platelet-derived growth factor–BB (10 ng/ml)] and incubated for 5 days as previously described (*26*). To obtain M-SMCs, CPC-SMCs were digested by Accutase, centrifuged, and seeded with the density of 1.5×10^4 cells/cm^2 in SMC maturation medium [DMEM/F12, 10% fetal bovine serum (FBS), and 1% penicillin-streptomycin] and incubated for 3 to 4 days until they reach 80 to 90% confluency.

BVGs were generated by culturing M-SMCs on biodegradable PGA-based scaffold as reported previously (*45*, *46*). The PGA mesh sheet (Confluent Medical Technologies Inc.) was cut to 1 cm by 4 cm and sewn around silicon tubing (2.0-mm outer diameter) to obtain a PGA scaffold. The PGA scaffold was first treated with 1.0 N sodium hydroxide (NaOH, Sigma-Aldrich) for 1 min, washed in deionized water three times, and immersed in 70% ethanol for 30 min. The scaffolds were then installed onto the needles in a 10-cm dish and dried overnight in a biological safety cabinet with the blower on and ultraviolet light off. The PGA scaffold was then coated with Matrigel (0.05 mg/mL) for 30 min and dried in a biological safety cabinet for 30 min. M-SMCs were seeded onto tubular PGA scaffold with the density of 15 million cells/ml and cultured in BVG medium [DMEM medium supplemented with 20% FBS, TGF-β1 (2 ng/ml), epidermal growth factor (0.5 ng/ml), basic fibroblast growth factor (10 ng/ml), Humulin (0.13 U/ml), 1% penicillin-streptomycin with additional proline (50 μg/ml), glycine (50 μg/ml), alanine (20 μg/ml), and $CuSO_4$ (3 ng/ml)]. After 1 week, the BVG media supplemented with ascorbic acid (50 μg/ml) was replaced twice a week. After 4 weeks of culture, the concentration of FBS was changed to 10%. After 8 weeks of culture, the BVGs were harvested under sterile conditions for in vitro mechanical tests and animal studies.

Implantation of BVGs into nude rats

To establish an in vivo animal model, we transplanted the BVGs as an interposition graft into the common carotid artery of *Foxn1*^{RNU} nude rats (strain code: 316, Charles River Laboratories). Experiments were performed on 3- to 4-month-old male nude rats. BVG pairs derived from *TGFBR1*$^{+/+}$ and *TGFBR1*$^{A230T/+}$ hiPSCs as well as *Patient*$^{A230T/+}$ and *Patient*$^{+/+}$ hiPSCs were implanted into the common carotid arteries of nude rats. Left and right common carotid arteries were carefully exposed and replaced with BVGs using a modified end-to-end cuff technique (*30*, *31*). After heparin was administrated intravenously, the common carotid artery was clamped proximally and distally, 3 to 4 cm apart. The common carotid artery was then divided in the middle between the clamps. An end-to-end anastomosis was made between the common carotid artery and BVG segments of 2 mm in inner diameter and 2 cm in length. The end-to-end rejoining was made by a 4-mm-long polyvinyl tube with a 1.1-mm diameter. The proximal part of the carotid artery was inserted into the tube, and the intimal side of the artery was everted. To fix the everted artery, another polyvinyl tube was inserted around the native artery and ligated using a 4-0 thin thread. Last, the cuff-mounted carotid artery was inserted into one end of BVGs. The same procedure was performed at the other end of BVGs with the other end of carotid artery. The BVG was flushed with saline solution before the graft was tied. The degree of anastomosis patency was confirmed by visualizing the pulsatile bright red blood flow in the transplanted BVGs after the vascular clamps were released. After confirmation of blood flow and hemostasis, the wound area was closed. We also performed unilateral BVG implantations for quantification purposes. The animals were monitored for 8 weeks. Enoxaparin was injected intraperitoneally daily to prevent thrombosis during the 8-week period (3 mg/kg). Although enoxaparin injections were efficient, we observed a rare complication of unilateral blood clot in one bilateral BVG implantation. In addition, we observed that BVG length was subjected to change during the 8-week period because of in vivo remodeling.

Statistical analysis

The quantitative BVG and tissue ring data were presented as means ± SD with at least four biological replicates. We conducted a Shapiro-Wilk normality test before all analyses. When analyzing more than two groups that were normally distributed, we tested for equal variance using the Brown-Forsythe test. If the STDs were not significantly different, we performed one-way analysis of variance (ANOVA) with Tukey's multiple comparison test to compare the mean of each column. When analyzing more than two groups that are not normally distributed, we performed nonparametric Kruskal-Wallis test with Dunn's multiple comparisons test. When analyzing only two datasets that were normally distributed, we used the two-tailed unpaired *t* test. If the variances were significantly different (*F* test), we conducted the two-tailed unpaired *t* test with Welch's correction. When analyzing two datasets that are not normally distributed, we used unpaired Mann-Whitney test. $P < 0.05$ was considered statistically significant. The statistical analyses were performed using the recommended tests by GraphPad Prism 9 Software.

Supplementary Materials

The PDF file includes:
Materials and Methods
Figs. S1 to S11
Tables S1 to S3

Other Supplementary Material for this manuscript includes the following:
Data files S1 and S2
MDAR Reproducibility Checklist

REFERENCES AND NOTES

1. H. Kuivaniemi, C. D. Platsoucas, M. D. Tilson, Aortic aneurysms. *Circulation* **117**, 242–252 (2008).
2. E. M. Isselbacher, Thoracic and abdominal aortic aneurysms. *Circulation* **111**, 816–828 (2005).
3. P. Danyi, J. A. Elefteriades, I. S. Jovin, Medical therapy of thoracic aortic aneurysms. *Circulation* **124**, 1469–1476 (2011).
4. D. M. Milewicz, D.-C. Guo, V. Tran-Fadulu, A. L. Lafont, C. L. Papke, S. Inamoto, C. S. Kwartler, H. Pannu, Genetic basis of thoracic aortic aneurysms and dissections: Focus

on smooth muscle cell contractile dysfunction. *Annu. Rev. Genomics Hum. Genet.* **9**, 283–302 (2008).
5. I. M. B. H. van de Laar, R. A. Oldenburg, G. Pals, J. W. Roos-Hesselink, B. M. de Graaf, J. M. A. Verhagen, Y. M. Hoedemaekers, R. Willemsen, L.-A. Severijnen, H. Venselaar, G. Vriend, P. M. Pattynama, M. Collée, D. Majoor-Krakauer, D. Poldermans, I. M. E. Frohn-Mulder, D. Micha, J. Timmermans, Y. Hilhorst-Hofstee, S. M. Bierma-Zeinstra, P. J. Willems, J. M. Kros, E. H. G. Oei, B. A. Oostra, M. W. Wessels, A. M. Bertoli-Avella, Mutations in SMAD3 cause a syndromic form of aortic aneurysms and dissections with early-onset osteoarthritis. *Nat. Genet.* **43**, 121–126 (2011).
6. A. Pinard, G. T. Jones, D. M. Milewicz, Genetics of thoracic and abdominal aortic diseases. *Circ. Res.* **124**, 588–606 (2019).
7. H. Sawada, J. Z. Chen, B. C. Wright, M. B. Sheppard, H. S. Lu, A. Daugherty, Heterogeneity of aortic smooth muscle cells: A determinant for regional characteristics of thoracic aortic aneurysms? *J. Transl. Int. Med.* **6**, 93–96 (2018).
8. H. Ji, H. S. Kim, H.-W. Kim, K. W. Leong, Application of induced pluripotent stem cells to model smooth muscle cell function in vascular diseases. *Curr. Opin. Biomed. Eng.* **1**, 38–44 (2017).
9. M. Shen, T. Quertermous, M. P. Fischbein, J. C. Wu, Generation of vascular smooth muscle cells from induced pluripotent stem cells. *Circ. Res.* **128**, 670–686 (2021).
10. M. Liu, D. Gomez, Smooth muscle cell phenotypic diversity. *Arterioscler. Thromb. Vasc. Biol.* **39**, 1715–1723 (2019).
11. G. K. Owens, M. S. Kumar, B. R. Wamhoff, Molecular regulation of vascular smooth muscle cell differentiation in development and disease. *Physiol. Rev.* **84**, 767–801 (2004).
12. A. Granata, F. Serrano, W. G. Bernard, M. McNamara, L. Low, P. Sastry, S. Sinha, An iPSC-derived vascular model of Marfan syndrome identifies key mediators of smooth muscle cell death. *Nat. Genet.* **49**, 97–109 (2017).
13. J. R. Bento, J. Meester, I. Luyckx, S. Peeters, A. Verstraeten, B. Loeys, The genetics and typical traits of thoracic aortic aneurysm and dissection. *Annu. Rev. Genomics Hum. Genet.* **23**, 223–253 (2022).
14. G. Ailawadi, C. W. Moehle, H. Pei, S. P. Walton, Z. Yang, I. L. Kron, C. L. Lau, G. K. Owens, Smooth muscle phenotypic modulation is an early event in aortic aneurysms. *J. Thorac. Cardiovasc. Surg.* **138**, 1392–1399 (2009).
15. E. G. MacFarlane, S. J. Parker, J. Y. Shin, B. E. Kang, S. G. Ziegler, T. J. Creamer, R. Bagirzadeh, D. Bedja, Y. Chen, J. F. Calderon, K. Weissler, P. A. Frischmeyer-Guerrerio, M. E. Lindsay, J. P. Habashi, H. C. Dietz, Lineage-specific events underlie aortic root aneurysm pathogenesis in Loeys-Dietz syndrome. *J. Clin. Invest.* **129**, 659–675 (2019).
16. L. Dobnikar, A. L. Taylor, J. Chappell, P. Oldach, J. L. Harman, E. Oerton, E. Dzierzak, M. R. Bennett, M. Spivakov, H. F. Jørgensen, Disease-relevant transcriptional signatures identified in individual smooth muscle cells from healthy mouse vessels. *Nat. Commun.* **9**, 4567 (2018).
17. M. E. DeBakey, D. H. Glaeser, Patterns of atherosclerosis: Effect of risk factors on recurrence and survival—analysis of 11,890 cases with more than 25-year follow-up. *Am. J. Cardiol.* **85**, 1045–1053 (2000).
18. H. Sawada, D. L. Rateri, J. J. Moorleghen, M. W. Majesky, A. Daugherty, Smooth muscle cells derived from second heart field and cardiac neural crest reside in spatially distinct domains in the media of the ascending aorta-brief report. *Arterioscler. Thromb. Vasc. Biol.* **37**, 1722–1726 (2017).
19. K. Takaluoma, M. Hyry, J. Lantto, R. Sormunen, R. A. Bank, K. I. Kivirikko, J. Myllyharju, R. Soininen, Tissue-specific changes in the hydroxylysine content and cross-links of collagens and alterations in fibril morphology in lysyl hydroxylase 1 knock-out mice. *J. Biol. Chem.* **282**, 6588–6596 (2007).
20. D. Wågsäter, V. Paloschi, R. Hanemaaijer, K. Hultenby, R. A. Bank, A. Franco-Cereceda, J. H. N. Lindeman, P. Eriksson, Impaired collagen biosynthesis and cross-linking in aorta of patients with bicuspid aortic valve. *J. Am. Heart Assoc.* **2**, e000034 (2013).
21. W. A. Cabral, W. Chang, A. M. Barnes, M. Weis, M. A. Scott, S. Leikin, E. Makareeva, N. V. Kuznetsova, K. N. Rosenbaum, C. J. Tifft, D. I. Bulas, C. Kozma, P. A. Smith, D. R. Eyre, J. C. Marini, Prolyl 3-hydroxylase 1 deficiency causes a recessive metabolic bone disorder resembling lethal/severe osteogenesis imperfecta. *Nat. Genet.* **39**, 359–365 (2007).
22. J. Hortop, P. Tsipouras, J. A. Hanley, B. J. Maron, J. R. Shapiro, Cardiovascular involvement in osteogenesis imperfecta. *Circulation* **73**, 54–61 (1986).
23. M. A. Whittle, P. S. Hasleton, J. C. Anderson, A. C. Gibbs, Collagen in dissecting aneurysms of the human thoracic aorta. Increased collagen content and decreased collagen concentration may be predisposing factors in dissecting aneurysms. *Am. J. Cardiovasc. Pathol.* **3**, 311–319 (1990).
24. R. J. Rizzo, W. J. McCarthy, S. N. Dixit, M. P. Lilly, V. P. Shively, W. R. Flinn, J. S. T. Yao, Collagen types and matrix protein content in human abdominal aortic aneurysms. *J. Vasc. Surg.* **10**, 365–373 (1989).
25. B. L. Loeys, U. Schwarze, T. Holm, B. L. Callewaert, G. H. Thomas, H. Pannu, J. F. De Backer, G. L. Oswald, S. Symoens, S. Manouvrier, A. E. Roberts, F. Faravelli, M. A. Greco, R. E. Pyeritz, D. M. Milewicz, P. J. Coucke, D. E. Cameron, A. C. Braverman, P. H. Byers, A. M. De Paepe, H. C. Dietz, Aneurysm syndromes caused by mutations in the TGF-β receptor. *N. Engl. J. Med.* **355**, 788–798 (2006).
26. D. Zhou, H. Feng, Y. Yang, T. Huang, P. Qiu, C. Zhang, T. R. Olsen, J. Zhang, Y. E. Chen, D. Mizrak, B. Yang, hiPSC modeling of lineage-specific smooth muscle cell defects caused byTGFBR1A230TVariant, and its therapeutic implications for Loeys-Dietz syndrome. *Circulation* **144**, 1145–1159 (2021).
27. S. L. M. Dahl, A. P. Kypson, J. H. Lawson, J. L. Blum, J. T. Strader, Y. Li, R. J. Manson, W. E. Tente, L. DiBernardo, M. T. Hensley, R. Carter, T. P. Williams, H. L. Prichard, M. S. Dey, K. G. Begelman, L. E. Niklason, Readily available tissue-engineered vascular grafts. *Sci. Transl. Med.* **3**, 68ra69 (2011).
28. J. Luo, L. Qin, L. Zhao, L. Gui, M. W. Ellis, Y. Huang, M. H. Kural, J. A. Clark, S. Ono, J. Wang, Y. Yuan, S.-M. Zhang, X. Cong, G. Li, M. Riaz, C. Lopez, A. Hotta, S. Campbell, G. Tellides, A. Dardik, L. E. Niklason, Y. Qyang, Tissue-engineered vascular grafts with advanced mechanical strength from human iPSCs. *Cell Stem Cell* **26**, 251–261.e8 (2020).
29. G. Konig, T. N. McAllister, N. Dusserre, S. A. Garrido, C. Iyican, A. Marini, A. Fiorillo, H. Avila, W. Wystrychowski, K. Zagalski, M. Maruszewski, A. L. Jones, L. Cierpka, L. M. de la Fuente, N. L'Heureux, Mechanical properties of completely autologous human tissue engineered blood vessels compared to human saphenous vein and mammary artery. *Biomaterials* **30**, 1542–1550 (2009).
30. S. Cho, I. H. Song, Cuff technique for small-diameter vascular grafts in the systemic arterial circulation of the rat. *Korean J. Thorac. Cardiovasc. Surg.* **51**, 423–426 (2018).
31. R. Oberhuber, B. Cardini, M. Kofler, P. Ritschl, R. Oellinger, F. Aigner, R. Sucher, S. Schneeberger, J. Pratschke, G. Brandacher, M. Maglione, Murine cervical heart transplantation model using a modified cuff technique. *J. Vis. Exp.*, e50753 (2014).
32. Ö. Önbaş, Ş. Dane, M. Kantarci, M. Koplay, F. Alper, A. Okur, Clinical importance of asymmetry and handedness differences in common carotid artery intima-media thickness. *Int. J. Neurosci.* **117**, 433–441 (2007).
33. R. He, D.-C. Guo, A. L. Estrera, H. J. Safi, T. T. Huynh, Z. Yin, S.-N. Cao, J. Lin, T. Kurian, L. M. Buja, Y.-J. Geng, D. M. Milewicz, Characterization of the inflammatory and apoptotic cells in the aortas of patients with ascending thoracic aortic aneurysms and dissections. *J. Thorac. Cardiovasc. Surg.* **131**, 671–678.e2 (2006).
34. I. El-Hamamsy, M. H. Yacoub, Cellular and molecular mechanisms of thoracic aortic aneurysms. *Nat. Rev. Cardiol.* **6**, 771–786 (2009).
35. Y. Hao, S. Hao, E. Andersen-Nissen, W. M. Mauck, S. Zheng, A. Butler, M. J. Lee, A. J. Wilk, C. Darby, M. Zager, P. Hoffman, M. Stoeckius, E. Papalexi, E. P. Mimitou, J. Jain, A. Srivastava, T. Stuart, L. M. Fleming, B. Yeung, A. J. Rogers, J. M. McElrath, C. A. Blish, R. Gottardo, P. Smibert, R. Satija, Integrated analysis of multimodal single-cell data. *Cell* **184**, 3573–3587.e29 (2021).
36. T. Palao, L. Medzikovic, C. Rippe, S. Wanga, C. Al-Mardini, A. van Weert, J. de Vos, N. N. van der Wel, H. A. van Veen, E. T. van Bavel, K. Swärd, V. de Waard, E. N. T. P. Bakker, Thrombospondin-4 mediates cardiovascular remodelling in angiotensin II-induced hypertension. *Cardiovasc. Pathol.* **35**, 12–19 (2018).
37. A. Subramanian, P. Tamayo, V. K. Mootha, S. Mukherjee, B. L. Ebert, M. A. Gillette, A. Paulovich, S. L. Pomeroy, T. R. Golub, E. S. Lander, J. P. Mesirov, Gene set enrichment analysis: A knowledge-based approach for interpreting genome-wide expression profiles. *Proc. Natl. Acad. Sci. U.S.A.* **102**, 15545–15550 (2005).
38. L. C. U. Junqueira, G. Bignolas, R. R. Brentani, Picrosirius staining plus polarization microscopy, a specific method for collagen detection in tissue sections. *Histochem. J.* **11**, 447–455 (1979).
39. D. Dayan, Y. Hiss, A. Hirshberg, J. J. Bubis, M. Wolman, Are the polarization colors of Picrosirius red-stained collagen determined only by the diameter of the fibers? *Histochemistry* **93**, 27–29 (1989).
40. D. Schepers, G. Tortora, H. Morisaki, G. MacCarrick, M. Lindsay, D. Liang, S. G. Mehta, J. Hague, J. Verhagen, I. van de Laar, M. Wessels, Y. Detisch, M. van Haelst, A. Baas, K. Lichtenbelt, K. Braun, D. van der Linde, J. Roos-Hesselink, G. McGillivray, J. Meester, I. Maystadt, P. Coucke, E. El-Khoury, S. Parkash, B. Diness, L. Risom, I. Scurr, Y. Hilhorst-Hofstee, T. Morisaki, J. Richer, J. Desir, M. Kempers, A. L. Rideout, G. Horne, C. Bennett, E. Rahikkala, G. Vandeweyer, M. Alaerts, A. Verstraeten, H. Dietz, L. Van Laer, B. Loeys, A mutation update on the LDS-associated genes TGFB2/3 and SMAD2/3. *Hum. Mutat.* **39**, 621–634 (2018).
41. M. E. Lindsay, H. C. Dietz, Lessons on the pathogenesis of aneurysm from heritable conditions. *Nature* **473**, 308–316 (2011).
42. I. Y. Chen, E. Matsa, J. C. Wu, Induced pluripotent stem cells: At the heart of cardiovascular precision medicine. *Nat. Rev. Cardiol.* **13**, 333–349 (2016).
43. J. Ozsvar, C. Yang, S. A. Cain, C. Baldock, A. Tarakanova, A. S. Weiss, Tropoelastin and elastin assembly. *Front. Bioeng. Biotechnol.* **9**, 643110 (2021).
44. B. L. Loeys, H. C. Dietz, A. C. Braverman, B. L. Callewaert, J. De Backer, R. B. Devereux, Y. Hilhorst-Hofstee, G. Jondeau, L. Faivre, D. M. Milewicz, R. E. Pyeritz, P. D. Sponseller, P. Wordsworth, A. M. De Paepe, The revised Ghent nosology for the Marfan syndrome. *J. Med. Genet.* **47**, 476–485 (2010).
45. L. Gui, B. C. Dash, J. Luo, L. Qin, L. Zhao, K. Yamamoto, T. Hashimoto, H. Wu, A. Dardik, G. Tellides, L. E. Niklason, Y. Qyang, Implantable tissue-engineered blood vessels from human induced pluripotent stem cells. *Biomaterials* **102**, 120–129 (2016).
46. L. E. Niklason, J. Gao, W. M. Abbott, K. K. Hirschi, S. Houser, R. Marini, R. Langer, Functional arteries grown in vitro. *Science* **284**, 489–493 (1999).

47. L. Chang, L. Villacorta, J. Zhang, M. T. Garcia-Barrio, K. Yang, M. Hamblin, S. E. Whitesall, L. G. D'Alecy, Y. E. Chen, Vascular smooth muscle cell–selective peroxisome proliferator–activated receptor-γ deletion leads to hypotension. *Circulation* **119**, 2161–2169 (2009).
48. T. Nilsson, J. Longmore, D. Shaw, E. Pantev, J. A. Bard, T. Branchek, L. Edvinsson, Characterisation of 5-HT receptors in human coronary arteries by molecular and pharmacological techniques. *Eur. J. Pharmacol.* **372**, 49–56 (1999).
49. Z. H. Yang, V. Richard, L. von Segesser, E. Bauer, P. Stulz, M. Turina, T. F. Luscher, Threshold concentrations of endothelin-1 potentiate contractions to norepinephrine and serotonin in human arteries. A new mechanism of vasospasm? *Circulation* **82**, 188–195 (1990).
50. B. C. Dash, K. Levi, J. Schwan, J. Luo, O. Bartulos, H. Wu, C. Qiu, T. Yi, Y. Ren, S. Campbell, M. W. Rolle, Y. Qyang, Tissue-engineered vascular rings from human iPSC-derived smooth muscle cells. *Stem Cell Rep.* **7**, 19–28 (2016).
51. N. O. Abutaleb, G. A. Truskey, Human iPSCs stretch to improve tissue-engineered vascular grafts. *Cell Stem Cell* **26**, 136–137 (2020).
52. B.-S. Kim, J. Nikolovski, J. Bonadio, D. J. Mooney, Cyclic mechanical strain regulates the development of engineered smooth muscle tissue. *Nat. Biotechnol.* **17**, 979–983 (1999).
53. J. Oller, E. Gabande-Rodriguez, M. J. Ruiz-Rodriguez, G. Desdin-Mico, J. F. Aranda, R. Rodrigues-Diez, C. Ballesteros-Martinez, E. M. Blanco, R. Roldan-Montero, P. Acuna, A. Forteza Gil, C. E. Martin-Lopez, J. F. Nistal, C. L. Lino Cardenas, M. E. Lindsay, J. L. Martin-Ventura, A. M. Briones, J. M. Redondo, M. Mittelbrunn, Extracellular tuning of mitochondrial respiration leads to aortic aneurysm. *Circulation* **143**, 2091–2109 (2021).
54. I. van der Pluijm, J. Burger, P. M. van Heijningen, A. IJpma, N. van Vliet, C. Milanese, K. Schoonderwoerd, W. Sluiter, L. J. Ringuette, D. H. W. Dekkers, I. Que, E. L. Kaijzel, L. Te Riet, E. G. MacFarlane, D. Das, R. van der Linden, M. Vermeij, J. A. Demmers, P. G. Mastroberardino, E. C. Davis, H. Yanagisawa, H. C. Dietz, R. Kanaar, J. Essers, Decreased mitochondrial respiration in aneurysmal aortas of Fibulin-4 mutant mice is linked to PGC1A regulation. *Cardiovasc. Res.* **114**, 1776–1793 (2018).
55. J. M. A. Verhagen, J. Burger, J. A. Bekkers, A. T. den Dekker, J. H. von der Thusen, M. Zajec, H. T. Bruggenwirth, M. L. T. van der Sterre, M. van den Born, T. M. Luider, W. F. J. van IJcken, M. W. Wessels, J. Essers, J. W. Roos-Hesselink, I. van der Pluijm, I. van de Laar, E. Brosens, Multi-omics profiling in Marfan Syndrome: Further insights into the molecular mechanisms involved in aortic disease. *Int. J. Mol. Sci.* **23**, 438 (2022).
56. J. J. Doyle, A. J. Doyle, N. K. Wilson, J. P. Habashi, D. Bedja, R. E. Whitworth, M. E. Lindsay, F. Schoenhoff, L. Myers, N. Huso, S. Bachir, O. Squires, B. Rusholme, H. Ehsan, D. Huso, C. J. Thomas, M. J. Caulfield, J. E. Van Eyk, D. P. Judge, H. C. Dietz; GenTAC Registry Consortium, and MIBAVA Leducq Consortium, A deleterious gene-by-environment interaction imposed by calcium channel blockers in Marfan syndrome. *eLife* **4**, e08648 (2015).
57. D. Langlois, M. Hneino, L. Bouazza, A. Parlakian, T. Sasaki, G. Bricca, J. Y. Li, Conditional inactivation of TGF-β type II receptor in smooth muscle cells and epicardium causes lethal aortic and cardiac defects. *Transgenic Res.* **19**, 1069–1082 (2010).
58. G. K. Owens, A. A. Geisterfer, Y. W. Yang, A. Komoriya, Transforming growth factor-beta-induced growth inhibition and cellular hypertrophy in cultured vascular smooth muscle cells. *J. Cell Biol.* **107**, 771–780 (1988).
59. S. Chen, R. J. Lechleider, Transforming growth factor-β-induced differentiation of smooth muscle from a neural crest stem cell line. *Circ. Res.* **94**, 1195–1202 (2004).
60. M. A. Perrella, M. K. Jain, M. E. Lee, Role of TGF-β in vascular development and vascular reactivity. *Miner. Electrolyte Metab.* **24**, 136–143 (1998).
61. F. Verrecchia, M. L. Chu, A. Mauviel, Identification of novel TGF-beta /Smad gene targets in dermal fibroblasts using a combined cDNA microarray/promoter transactivation approach. *J. Biol. Chem.* **276**, 17058–17062 (2001).
62. X. Dai, J. Shen, N. Priyanka Annam, H. Jiang, E. Levi, C. M. Schworer, G. Tromp, A. Arora, M. Higgins, X.-F. Wang, M. Yang, H. J. Li, K. Zhang, H. Kuivaniemi, L. Li, SMAD3 deficiency promotes vessel wall remodeling, collagen fiber reorganization and leukocyte infiltration in an inflammatory abdominal aortic aneurysm mouse model. *Sci. Rep.* **5**, 10180 (2015).
63. M. Gnoli, E. Brizola, M. Tremosini, E. Pedrini, M. Maioli, M. Mosca, A. Bassotti, P. Castronovo, C. Giunta, L. Sangiorgi, COL1-related disorders: Case report and review of overlapping syndromes. *Front. Genet.* **12**, 640558 (2021).
64. J. A. N. Meester, A. Verstraeten, D. Schepers, M. Alaerts, L. Van Laer, B. L. Loeys, Differences in manifestations of marfan syndrome, ehlers-danlos syndrome, and loeys-dietz syndrome. *Ann. Cardiothorac. Surg.* **6**, 582–594 (2017).
65. O. Rahkonen, M. Su, H. Hakovirta, I. Koskivirta, S. G. Hormuzdi, E. Vuorio, P. Bornstein, R. Penttinen, Mice with a deletion in the first intron of thecol1a1gene develop age-dependent aortic dissection and rupture. *Circ. Res.* **94**, 83–90 (2004).
66. R. Vroman, A.-M. Malfait, R. E. Miller, F. Malfait, D. Syx, Animal models of ehlers–danlos syndromes: Phenotype, pathogenesis, and translational potential. *Front. Genet.* **12**, 726474 (2021).
67. C. J. Bowen, J. F. Calderón Giadrosic, Z. Burger, G. Rykiel, E. C. Davis, M. R. Helmers, K. Benke, E. Gallo MacFarlane, H. C. Dietz, Targetable cellular signaling events mediate vascular pathology in vascular Ehlers-Danlos syndrome. *J. Clin. Invest.* **130**, 686–698 (2020).
68. U. Schwarze, W. I. Schievink, E. Petty, M. R. Jaff, D. Babovic-Vuksanovic, K. J. Cherry, M. Pepin, P. H. Byers, Haploinsufficiency for one COL3A1 allele of type iii procollagen results in a phenotype similar to the vascular form of Ehlers-Danlos syndrome, Ehlers-Danlos syndrome type IV. *Am. J. Hum. Genet.* **69**, 989–1001 (2001).
69. A. W. den Hartog, R. Franken, A. H. Zwinderman, J. Timmermans, A. J. Scholte, M. P. van den Berg, V. de Waard, G. Pals, B. J. Mulder, M. Groenink, The risk for type B aortic dissection in Marfan syndrome. *J. Am. Coll. Cardiol.* **65**, 246–254 (2015).
70. M. E. Lindsay, H. C. Dietz, The genetic basis of aortic aneurysm. *Cold Spring Harb. Perspect. Med.* **4**, a015909 (2014).
71. Z. Szabo, M. W. Crepeau, A. L. Mitchell, M. J. Stephan, R. A. Puntel, K. Yin Loke, R. C. Kirk, Z. Urban, Aortic aneurysmal disease and cutis laxa caused by defects in the elastin gene. *J. Med. Genet.* **43**, 255–258 (2006).
72. J. Barallobre-Barreiro, B. Loeys, M. Mayr, M. Rienks, A. Verstraeten, J. C. Kovacic, Extracellular matrix in vascular disease, Part 2/4: JACC focus seminar. *J. Am. Coll. Cardiol.* **75**, 2189–2203 (2020).
73. D. Eyre, P. Shao, M. Ann Weis, B. Steinmann, The kyphoscoliotic type of Ehlers–Danlos syndrome (type VI): Differential effects on the hydroxylation of lysine in collagens I and II revealed by analysis of cross-linked telopeptides from urine. *Mol. Genet. Metab.* **76**, 211–216 (2002).
74. C. Giunta, A. Randolph, B. Steinmann, Mutation analysis of the PLOD1 gene: An efficient multistep approach to the molecular diagnosis of the kyphoscoliotic type of Ehlers-Danlos syndrome (EDS VIA). *Mol. Genet. Metab.* **86**, 269–276 (2005).
75. S. N. Koenig, O. Cavus, J. Williams, M. Bernier, J. Tonniges, H. Sucharski, T. Dew, M. Akel, P. Baker, F. Madiai, F. De Giorgi, L. Scietti, S. Faravelli, F. Forneris, P. J. Mohler, E. A. Bradley, New mechanistic insights to PLOD1-mediated human vascular disease. *Transl. Res.* **239**, 1–17 (2022).
76. M. Renard, C. Francis, R. Ghosh, A. F. Scott, P. D. Witmer, L. C. Adès, G. U. Andelfinger, P. Arnaud, C. Boileau, B. L. Callewaert, D. Guo, N. Hanna, M. E. Lindsay, H. Morisaki, T. Morisaki, N. Pachter, L. Robert, L. Van Laer, H. C. Dietz, B. L. Loeys, D. M. Milewicz, J. De Backer, Clinical validity of genes for heritable thoracic aortic aneurysm and dissection. *J. Am. Coll. Cardiol.* **72**, 605–615 (2018).
77. M. Balasubramanian, A. Verschueren, S. Kleevens, I. Luyckx, M. Perik, S. Schirwani, G. Mortier, H. Morisaki, I. Rodrigus, L. Van Laer, A. Verstraeten, B. Loeys, Aortic aneurysm/dissection and osteogenesis imperfecta: Four new families and review of the literature. *Bone* **121**, 191–195 (2019).
78. P. Arnaud, Z. Mougin, C. Boileau, C. Le Goff, Cooperative mechanism of ADAMTS/ADAMTSL and fibrillin-1 in the Marfan syndrome and acromelic dysplasias. *Front. Genet.* **12**, 734718 (2021).
79. T. Kilic, K. Okuno, S. Eguchi, Z. Kassiri, Disintegrin and metalloproteinases (ADAMs [A disintegrin and metalloproteinase] and ADAMTSs [ADAMs with a thrombospondin motif]) in aortic aneurysm. *Hypertension* **79**, 1327–1338 (2022).
80. F. Malfait, Vascular aspects of the Ehlers-Danlos Syndromes. *Matrix Biol.* **71-72**, 380–395 (2018).
81. L. Gui, L. Zhao, R. W. Spencer, A. Burghouwt, M. S. Taylor, S. W. Shalaby, L. E. Niklason, Development of novel biodegradable polymer scaffolds for vascular tissue engineering. *Tissue Eng. Part A* **17**, 1191–1200 (2011).
82. C. Quint, Y. Kondo, R. J. Manson, J. H. Lawson, A. Dardik, L. E. Niklason, Decellularized tissue-engineered blood vessel as an arterial conduit. *Proc. Natl. Acad. Sci. U.S.A.* **108**, 9214–9219 (2011).
83. J. H. Eoh, N. Shen, J. A. Burke, S. Hinderer, Z. Xia, K. Schenke-Layland, S. Gerecht, Enhanced elastin synthesis and maturation in human vascular smooth muscle tissue derived from induced-pluripotent stem cells. *Acta Biomater.* **52**, 49–59 (2017).
84. H. Sugitani, H. Wachi, S. Tajima, Y. Seyama, Nitric oxide stimulates elastin expression in chick aortic smooth muscle cells. *Biol. Pharm. Bull.* **24**, 461–464 (2001).
85. K. Noda, B. Dabovic, K. Takagi, T. Inoue, M. Horiguchi, M. Hirai, Y. Fujikawa, T. O. Akama, K. Kusumoto, L. Zilberberg, L. Y. Sakai, K. Koli, M. Naitoh, H. von Melchner, S. Suzuki, D. B. Rifkin, T. Nakamura, Latent TGF-β binding protein 4 promotes elastic fiber assembly by interacting with fibulin-5. *Proc. Natl. Acad. Sci. U.S.A.* **110**, 2852–2857 (2013).
86. N. F. Tojais, A. Cao, Y.-J. Lai, L. Wang, P.-I. Chen, M. A. A. Alcazar, V. de Jesus Perez, R. K. Hopper, C. J. Rhodes, M. A. Bill, L. Y. Sakai, M. Rabinovitch, Codependence of bone morphogenetic protein receptor 2 and transforming growth factor-β in elastic fiber assembly and its perturbation in pulmonary arterial hypertension. *Arterioscler. Thromb. Vasc. Biol.* **37**, 1559–1569 (2017).
87. B. L. Wolfe, C. B. Rich, H. D. Goud, A. J. Terpstra, M. Bashir, J. Rosenbloom, G. E. Sonenshein, J. A. Foster, Insulin-like growth factor-I regulates transcription of the elastin gene. *J. Biol. Chem.* **268**, 12418–12426 (1993).

Acknowledgments: We are grateful to K. Converso-Baran of University of Michigan Frankel Cardiovascular Center and Department of Molecular & Integrative Physiology Phenotyping Core for ultrasound test and analysis and K. Poli of Mechanical Engineering for mechanical test and analysis. We also thank the University of Michigan Advanced Genomics Core for performing spatial transcriptomics profiling of vascular grafts. **Funding:** This study was

supported by NIH grants HL130614, HL141891, and HL151776 to B.Y.; HL109946, HL134569, and HL159871 to Y.E.C.; HL138139, HL153710, and GM122181 to J. Z.; and American Heart Association Postdoctoral Fellowship 22POST830938 to Y.Y. **Author contributions:** Conceptualization of this work was performed by Y.E.C., D.M., and B.Y. The methodology for this work was advised by J.Z., P.Q., L.C., Y.E.C., D.M., and B.Y. The methodology for this work was performed by Y.Y., H.F., Y.T., P.Q., Z.W., L.C., and D.M. The in vivo rat experiments were performed by Y.Y. and advised by X.H. The project administration was managed by B.Y. Funding was acquired by Y.Y., J.Z., Y.E.C., and B.Y. The project was supervised by Y.E.C., D.M., and B.Y. The original draft of this manuscript was written by Y.Y., B.Y., and D.M. Reviewing and editing of this manuscript were done by Y.Y., Y.E.C., D.M., and B.Y. **Competing interests:** The authors declare that they have no competing interests. **Data and materials availability:** All data associated with this study are present in the paper or the Supplementary Materials. Human-derived study materials can be made available from the corresponding authors with Institutional Review Board approval and a material transfer agreement. The raw and processed spatial transcriptomics data have been deposited to the Gene Expression Omnibus database under the accession number GSE216992.

Submitted 10 January 2023
Resubmitted 15 June 2023
Accepted 17 April 2024
Published 8 May 2024
10.1126/scitranslmed.adg6298